Very large amplitude vibrations of flexible structures: experimental identification and validation of a quadratic drag damping model

Mathieu Colin, Olivier Thomas, Sébastien Grondel, Eric Cattan

Very Large Amplitude Vibrations of Flexible Structures: Experimental identification and validation of a quadratic drag damping model

Mathieu Colin[a,*], Olivier Thomas[a], Sébastien Grondel[b] and Eric Cattan[b]

[a]*Arts et Métiers, LISPEN EA 7515, 8 Boulevard Louis XIV, 59046 Lille, France*
[b]*Univ. Polytechnique Hauts-de-France, CNRS, Univ. Lille, ISEN, Centrale Lille, UMR 8520 - IEMN-DOAE, F-59313 Valenciennes, France*

ARTICLE INFO

Abstract

This article presents a theoretical, numerical and experimental study of resonant structures undergoing very large amplitude vibrations. The purpose of this work is to validate a model for the damping due to the action of the air on a structure's single-mode response in the steady-state. Experiments are performed on cantilever beams and beam assemblies of various sizes, from centimetric to micrometric, under harmonic base excitation. Dimensionless linear and nonlinear modal damping coefficients are simultaneously identified by means of frequency-domain identification techniques. These measurements demonstrate the pertinence of the presented model.

Introduction

When a flexible structure is subjected to large amplitude vibrations, numerous nonlinear phenomena take place. The vast literature on geometric nonlinearities helps to understand the peculiar effects (such as coexisting possibly stable and unstable solutions, bifurcations, strong exchanges of energy between vibration modes and chaotic responses, see [Nayfeh and Mook, 1979; Thomas et al., 2007; Touzé et al., 2011; Cadot et al., 2016]), through the use of various models. However, most of the available studies include linear only damping models, whereas nonlinear damping effects, associated with large amplitude vibrations, are often observed experimentally and have been – relatively – overlooked. In this context, this work presents the theoretical background and identification procedure of a nonlinear modal damping model adapted to thin structures undergoing very large amplitude vibrations.

The recrudescence of studies on nonlinear damping stresses the interest in this topic, regarding structures of all sizes. In the field of micro/nano-electro-mechanical systems (M/NEMS), nonlinear damping effects have been observed for some time [Younis, 2010; Eichler et al., 2011], with only a handful of studies delving into modelling the experimental observations (e.g. [Zaitsev et al., 2012]). In the case of macro-scale structures, the dependance of the damping on the amplitude has been previously reported in the literature for plates and shells (see e.g. the experiments reported in Alijani et al. [2016]; Amabili et al. [2016] and Figs. 14, 15, 16 of Thomas et al. [2007] in which a model with a linear viscous damping becomes inaccurate at large amplitude). In a recent series of studies, this effect is attributed to the joint contribution of viscoelasticity and geometrical nonlinearities, addressed both theoretically and experimentally in the case of plate and shells in Balasubramanian et al. [2018]; Amabili [2018a,b, 2019].

On the other side of the size spectrum for man-made structures, a few studies in the field of civil engineering illustrate that including the aerodynamic damping in the design of high-rise buildings is critical [Zhang et al., 2019]. Structures for which a nonlinear damping model could be valuable (but has not yet been studied) are micro and nano aerial vehicles (M/NAV). As the size of the system decreases, the ratio of

---

*Corresponding author
✉ mathieu.r.colin@gmail.com (M. Colin); olivier.thomas@ensam.eu (O. Thomas); sebastien.grondel@uphf.fr (S. Grondel); eric.cattan@uphf.fr (E. Cattan)
ORCID(s): 0000-0003-3600-6415 (M. Colin); 0000-0001-7240-5259 (O. Thomas); 0000-0003-1542-9494 (S. Grondel); 0000-0002-6576-5800 (E. Cattan)

---

the surface forces over body forces increases [Rhoads et al., 2008]; air interaction has to be accounted for, thus justifying the need for a nonlinear damping model for air-induced damping in micro scale structures.

The motivation for this work is the design of a structure for which vibrations are desired: we aim to make a NAV take-off. This nano drone is described hereunder. It differentiates itself from the other NAVs with two main features. The first is the use of microfabrication techniques [Bontemps et al., 2013], that produce a fully flexible polymer structure (SU-8 for the frame and Parylene-C for the membrane). Its second characteristic is the lift generation mechanism, which does not rely on passive wing rotation, but on the combination of two vibration modes, a bending one and a twisting one, excited in phase quadrature by a harmonic point forcing [Faux et al., 2018]. The peculiar wing trajectory thus created replicates the dipteras' wing motion [Fry et al., 2003] and generates lift. Therefore, this nano drone is making use of an entirely flexible structure to activate the wings vibration, which justifies the novel denomination "vibrating-wing nano air vehicle" [VWNAV] [Doan et al., 2016]. The current prototypes achieve substantial vibrations amplitudes - around $30°$ of peak-to-peak flapping angle - and generate a lift equivalent to the drone's weight before the saturation of the actuator. Aiming at increasing this flapping amplitude, a refinement of our existing design model and a deeper understanding of the damping effects of the surrounding fluid are needed. This article addresses these points by considering structures with a gradual complexity, from simple cantilever beams of various sizes to VWNAV wing prototypes.

Damping is the manifestation of the effects of various phenomena dissipating energy within an oscillating system: internal dissipation within the material (thermoelastic and viscoelastic damping [Chaigne and Lambourg, 2001; Schmid and Hierold, 2008; Amabili, 2019]), fluid-structure interaction (squeeze-film [Hosaka et al., 1995], air flow damping [Hosaka and Itao, 1999; Nouira et al., 2007], and acoustic radiation [Chaigne and Lambourg, 2001]), or imperfect boundary conditions (such as clamping loss [Hao et al., 2003; Chouvion et al., 2012] or friction in joints [Dion et al., 2013]). Due to its many possible sources, including damping in a model is not straightforward and many models include linear modal terms which coefficients are experimentally estimated. This uncoupled modal model is theoretically justified if the damping is low, for linear (low amplitude) vibrations (see e.g. [Géradin and Rixen, 1994]). In the case of the tested structures of this article, we assume that for small amplitude vibrations those assumptions are valid and that a linear damping term embeds all the above physical sources of damping. This is further justified by the weakly viscoelastic behaviour of the materials of the tested structures (high-yield steel and SU-8, which has a loss modulus about 40 times smaller than the storage modulus at the frequency and temperature ranges of interest [Schmid and Hierold, 2008; Le Rouzic et al., 2009]). For larger amplitude of vibrations, we identified that the interaction with the surrounding fluid, which leads to quadratic nonlinear terms in the equations, is a predominant damping effect. Other nonlinear damping sources, such as viscoelastic effects combined with geometrical nonlinearities can also have an effect, but at a higher (cubic) order. This article mainly addresses the use and the effect of a quadratic damping term due to the interaction of the structure vibrations with the air flow, and verify experimentally that it is predominant for the tested structures.

Many models for air interaction exist, with varying degrees of complexity. A basic approach is to consider that the force applied to the structure by the fluid can be separated into two components: (i) a conservative *added mass* term, proportional to an acceleration term (which effect is mainly to decrease the natural frequency), and (ii) a *drag damping* term, depending on the velocity [Keulegan and Carpenter, 1958]. The underlying hypothesis for this "structural" approach is to consider a steady (or quasi-steady) flow for the surrounding fluid. When this hypothesis is not verified, more advanced approaches are required. Indeed, as unsteady flows produce complex phenomena (such as the *Wagner effect* or the *Magnus effect*, related to respectively the delayed stall and the rotational circulation – two lift generating mechanisms for insects during the flapping cycle [Dickinson et al., 1999]), the corresponding fluid loads are very diverse [Bidkar et al., 2009]. In this approach, the vast majority of the models requires a numerical solver for the Navier-Stokes equations [Aureli and Porfiri, 2010; Phan et al., 2013]. The analytical models proposed in [Ansari et al., 2006; Pedersen and Żbikowski, 2006] are noteworthy as they provide analytical aerodynamic models accounting for quasi-steady and unsteady flows (in the context of the development of a MAV). The simulations perform well on the experimental data from [Sane and Dickinson, 2001], but the model applies to rigid plates.

A general expression of fluid-induced damping is in the form: $c|v^{n-1}(t)|v(t)$, with c a scalar and v the velocity of the structure with respect to the surrounding media. The case $n = 1$ is the linear – or Stokes –

model and $n = 0$ can be related to dry friction [Géradin and Rixen, 1994]. The most usual model for the aerodynamic drag is $n = 2$ [Anderson et al., 1996; Malatkar and Nayfeh, 2003; Egorov et al., 2018]. The case $n = 3$ (equivalent to cv^3) can also be found in the literature to model the damping due to air on a structure [Gottlieb and Habib, 2012; Zaitsev et al., 2012]. It originates in investigations on ship roll damping equivalents (see [Haddara, 1973; Dalzell, 1976; Bikdash et al., 1993]), as the case $n = 2$ is mathematically strenuous to use when the structure's dynamic response involves more than one mode (which is the case for the random excitation of waves on a ship). Although independent of fluid-induced damping, the study [Elliott et al., 2015] provides a detailed analytical and numerical study on the general $c_n|v^{n-1}(t)|v(t)$ model. It proposes several examples in the literature and formulates an equivalent damping obtained by retaining the fundamental term in a harmonic balance analysis.

The topic of identification of nonlinear systems is vast and covers many applications [Kerschen et al., 2006], but there are few techniques to identify nonlinear damping in the steady state, and even fewer techniques use the frequency domain [Doughty et al., 2002]. Model-based frequency-domain identification techniques are mostly due to Pr. Nayfeh's team work. For cantilever beams, one can refer to [Nayfeh, 1985] and especially [Krauss and Nayfeh, 1999; Malatkar and Nayfeh, 2003], applied to single-mode responses of weakly nonlinear structures. The model includes nonlinear damping in the form of $cv|v|$, and measurements are made on third and fourth modes of a macroscopic steel beam. In [Malatkar and Nayfeh, 2003], the parametric identification consists in a frequency response curve-fitting, whereas in [Krauss and Nayfeh, 1999], the technique is based on curve-fitting fixed points of the system. These studies are of utmost importance since they present a model that distinguishes the linear and quadratic modal damping coefficients, and take into account geometric nonlinearities that arise when the amplitude of motion is large.

The geometric nonlinearities of a cantilever beam have been studied analytically in the seminal article [Crespo da Silva and Glynn, 1978]. It establishes the equations of motion of bending (about two principal axes) and torsion of an inextensional beam through an expansion in Taylor series truncated at order 3. From there, [Pai and Nayfeh, 1990] demonstrated that the first mode presents a slightly hardening behaviour, which was confirmed later on in several publications. This hardening behaviour manifests itself by a shift of the frequency response towards the high frequencies as the amplitude increases. Yet, the critical review [Sabater and Rhoads, 2017] apprises of the possible errors that third-order geometric nonlinearity approximation can engender on parametric system identification techniques using perturbation methods in resonant micro/nano systems. In particular, for a linearly damped microresonator, fifth-order simulations show that the normalised amplitude at resonance decreases as the forcing amplitude increases, which would be caused by the geometric nonlinearities.

The core contributions of this work are the determination of a nonlinear damping model for the effect of air-induced damping in the steady-state vibration of cantilever structures and the presentation of a novel identification technique. This paper is organised as follows. Section 1 presents the linear beam model, which serves to identify key parameters in obtaining large amplitude vibration, as well as the nonlinear beam model including the geometric nonlinearities. The second section presents the nonlinear damping model, inspired from [Krauss and Nayfeh, 1999; Malatkar and Nayfeh, 2003], comparing it in subsection 2.3 to other nonlinear damping models in use, and validating its parametric identification in subsection 2.4. Next, section 3 presents the materials and methods used for the experimental identification. The section 4 presents the experimental results and discusses the identified damping coefficients and the procedure.

1. Theory

In this section, we consider a cantilever beam because analytical models, either for linear and geometrically nonlinear vibrations, are at hand and very realistic. Our purpose is to introduce all our methodology and highlight all parameters relevant to obtain very large amplitudes of vibration. We first recall the linear model of the beam, which is then enriched with nonlinear terms accounting for geometric nonlinearities before adding nonlinear damping terms in the next section.

We consider a straight cantilever beam of length L with a uniform cross-section of area S and second moment of area I, made of a homogeneous and isotropic elastic material of density ρ and Young's modulus E. We restrict our attention to transverse vibrations in one direction only. The considered models are based on the classical Euler-Bernoulli kinematics, for which each cross-section is rigid and remains orthogonal to

the neutral line. The transverse displacement of the cross-section at abscissa x and time t is written $w(x,t)$.

1.1. Linear beam model

In this section, we first consider the classical linear model for the cantilever beam. In this case, $w(x,t)$ verifies the following equation:

$$EIw'''' + \rho S \ddot{w} = p, \tag{1}$$

where p is the load per unit length and $\bullet' = \partial \bullet /\partial x$ and $\dot{\bullet} = \partial \bullet /\partial t$. It is then convenient to rewrite Eq. (1) in a dimensionless form. For that, we decide to set the length of the beam L as the characteristic length, leading to the following dimensionless quantities denoted by overbars:

$$\bar{x} = \frac{x}{L}; \quad \bar{w} = \frac{w}{L}; \quad \bar{p} = \frac{pL^3}{EI} \quad \text{and} \quad \bar{t} = \frac{t}{t_0} = \frac{t}{L^2}\sqrt{\frac{EI}{\rho S}} \tag{2}$$

Introducing Eqs. (2) into Eq. (1) yields:

$$\bar{w}'''' + \ddot{\bar{w}} = \bar{p}, \tag{3}$$

where, when applied to dimensionless quantities, $\bar{\bullet}' = \partial \bar{\bullet}/\partial \bar{x}$ and $\dot{\bar{\bullet}} = \partial \bar{\bullet}/\partial \bar{t}$.

The natural modes of the beam $(\omega_k, \Phi_k(\bar{x}))$ are solutions of the eigenvalue problem:

$$\Phi'''' - \omega_k^2 \Phi = 0. \tag{4}$$

with the following boundary conditions in the case of the cantilever beam:

$$\Phi(0) = 0; \quad \Phi'(0) = 0; \quad \Phi''(1) = 0; \quad \Phi'''(1) = 0. \tag{5}$$

The mode shapes are written as follows:

$$\Phi_k(\bar{x}) = \frac{1}{2}\left(\cosh\left(\beta_k\,\bar{x}\right) - \cos\left(\beta_k\,\bar{x}\right) + \frac{\cos\beta_k + \cosh\beta_k}{\sin\beta_k + \sinh\beta_k}\left(\sin\left(\beta_k\,\bar{x}\right) - \sinh\left(\beta_k\,\bar{x}\right)\right)\right), \tag{6}$$

and the dimensionless natural frequencies are $\omega_k = \beta_k^2$, where β_k is the k-th solution of $\cos\beta_k \cosh\beta_k + 1 = 0$. The first 4 values are:

$$\beta_1 = 1.8751, \quad \beta_2 = 4.6941, \quad \beta_3 = 7.8548, \quad \beta_4 = 10.996. \tag{7}$$

Besides, the normalisation of the mode shapes in Eq. (6) leads to $|\Phi_k(1)| = 1$, $\int_0^1 \Phi_k^2(\bar{x})\,\mathrm{d}\bar{x} = 1/4$, $\forall k \in \mathbb{N}^*$. Using the time constant t_0 of Eq. (2), the k-th. dimensioned frequency, in [Hz], verifies:

$$f_k = \frac{\omega_k}{2\pi t_0} = \frac{\beta_k^2}{2\pi L^2}\sqrt{\frac{EI}{\rho S}} = \frac{\beta_k^2}{4\sqrt{3}\pi}\frac{h}{L^2}\sqrt{\frac{E}{\rho}}, \tag{8}$$

where the last equation is valid in the case of a rectangular cross section of thickness h.

We expand the transverse displacement of the beam on the natural modes basis:

$$\bar{w}(\bar{x},\bar{t}) = \sum_{k=1}^{+\infty} \Phi_k(\bar{x})q_k(\bar{t}). \tag{9}$$

Substituting Eq. (9) into Eq. (3) and using the orthogonality properties of the modes leads to the following equations, for all $k \in \mathbb{N}^*$:

$$\ddot{q}_k + 2\xi_k\omega_k\dot{q}_k + \omega_k^2 q_k = Q_k, \tag{10}$$

where ξ_k is a linear modal damping factor added *a posteriori* and with

$$Q_k(\bar{t}) = \frac{\int_0^1 \Phi_k(\bar{x})\,\bar{p}(\bar{x},\bar{t})\,\mathrm{d}\bar{x}}{\int_0^1 \Phi_k^2(\bar{x})\,\mathrm{d}\bar{x}}. \tag{11}$$

1.2. Obtaining large amplitude vibrations

We address in this section the parameters of the considered thin structures that limit their maximum amplitude in vibration. This point is relevant in the case of our VWNAV, for which we want to increase as much as possible the vibrations amplitude in operating conditions. It is also of interest when designing a specific experimental test of vibrations of thin structures in very large amplitude, to estimate the limits under which one has to stay in order to avoid damaging or breaking the tested specimen. To obtain simple criteria, we focus on the linear model introduced in the previous section. Even if a cantilever beam is considered, the obtained results can be extended to more complex structures, provided they are thin, such as the beam assemblies of our VWNAV considered in the experimental sections 3, 4 of the present article and fully described in [Faux et al., 2019].

1.2.1. Maximum resonant amplitude criterion

Considering a beam of rectangular cross section (width b and thickness h), excited by a sine point forcing of dimensioned amplitude F_e (in [N]) at abscissa $\bar{x}_e$, and assuming a single-mode response for the displacement in Eq. (9), Eq. (10) leads to the expression of the modal coordinate amplitude at resonance ($\Omega \approx \omega_k$) and thus to the tip displacement of the beam (at $\bar{x} = 1$) as a function of the applied force:

$$\frac{w_{k,\mathrm{max}}}{L} = \underbrace{\frac{6\,\Phi_k(1)}{\beta_k^4 \int_0^1 \Phi_k^2(\bar{x})\,\mathrm{d}\bar{x}}}_{\mathrm{Modal}} \underbrace{\frac{L^2}{bh^3}}_{\mathrm{Geo.}} \underbrace{\frac{1}{E}}_{\mathrm{Mat.}} \underbrace{\frac{1}{\xi_k}}_{\mathrm{Damp.}} \underbrace{\Phi_k(\bar{x}_e)F_e}_{\mathrm{Forcing}}, \tag{12}$$

where the expression of $\bar{p}$ in Eq. (2) has been used.

Eq. (12) presents five independent terms originating from different types of contributions: the modal properties (that are inherent to the shape of the structure itself regardless of the dimensions), the geometric parameters (length and geometry of the cross-section), the material's properties, the damping ratio and the forcing itself. Moreover, even if the present equations are valid for a single cantilever beam, if the material is homogeneous, all interpretation can be easily extended to beam assemblies subjected to a point forcing (e.g. the VWNAV with its electromagnetic actuator [Faux et al., 2019]).

As a consequence, in order to maximise the tip (maximum) displacement of the structure at resonance, one can act on several of these contributions. First is the design of the geometry: the more slender the geometry is, the higher the vibrations amplitude is ($L \gg h, b$). The second lever is the choice of an appropriate material: it should be flexible (E low) but its intrinsic material damping should be low as well, to reduce ξ_k as much as possible. The damping ratio ξ_k also includes the effects of imperfect boundary conditions and air interaction; one has thus to limit the clamping losses by designing proper boundary conditions, the air losses being the subject of the remaining of this paper. The last lever is to maximise the forcing and select a forcing point $\bar{x}_e$ where the amplitude is high. In addition, one can remark that the index k of the mode has also an influence, gathered in the value of β_k (for the beam, $\Phi_k(1)$ and $\int_0^1 \Phi_k^2(\bar{x})\,\mathrm{d}\bar{x}$ are independent of k), that increases with the value of k (see Eqs. (7)). Consequently, for a given geometry, material, and damping ratio, the lower the mode is, the higher its amplitude at resonance is.

1.2.2. Yield limit criterion

When considering large amplitude vibrations, one should verify that the maximum stress in the beam domain σ is lower than the yield strength of the material σ_e, to avoid a non-reversible change of shape due to plasticity. Basic strength of material theory, based on the Euler-Bernoulli kinematics used in the model, gives $\sigma = -Mh/(2I)$, with the bending moment $M = EIw''$. Substituting into these equations the displacement from Eq. (9) on which is used the single-mode approximation, one can write the maximum displacement of a beam before yield:

$$\frac{w_{k,\mathrm{yield}}}{L} = \underbrace{\frac{2\Phi_k(1)}{\max_{\bar{x}}(\Phi_k'')}}_{\mathrm{Modal}} \underbrace{\frac{L}{h}}_{\mathrm{Geo.}} \underbrace{\frac{\sigma_e}{E}}_{\mathrm{Mat.}}. \tag{13}$$

Similar contributions to those identified in the previous criterion (Eq. (12)) can be highlighted here: the structure should be as slender ($L \gg h$) as possible, which concurs with the resonant criterion (although

width b is no longer determinant), and the dimensionless ratio σ_e/E should be as high as possible for the selected material.

1.2.3. Material selection remarks

	E [GPa]	ξ	σ_e [MPa]	Resonant criterion Eq. (12)	Yield criterion Eq. (13)
S235 steel	210	0.1%	235	1	1
Aluminium	70	0.1%	110 - 300*	3	1.4-3.8
High yield steel	175†	0.1%†	850 - 1200*	1.2	4.34-6.13
Silicon	170‡	0.1-1%‡	170 - 1700*	0.12-1.23	0.89-8.9
SU-8	4.88†	1%†	50 - 80*	**5.22**	**9.16-14.6**

Table 1
Comparison of different materials with maximum amplitude criteria.
†-noted values are extracted from measurements detailed in sections 3-4 assuming a perfect clamp boundary condition. ‡-noted values are extracted from [Naeli and Brand, 2009]. (* Yield strength values are estimated from manufacturers data sheets).

The two criteria introduced in the preceding sections stress the importance of the geometric design as well as the choice of the material. To illustrate the pertinence of choosing an apropriate material, we selected four different materials. The first material is a widely used S235 steel, which is chosen as the reference with base index 1. Then, aluminium, that has a smaller Young's modulus and a comparable yield limit, is considered. In addition, a high yield steel is also considered, to assess the benefit of choosing an enhanced material (on the second criterion in particular). As most MEMS are fabricated using silicon, it is interesting to see its potential compared to steel. Finally, the SU-8 – an epoxy-based photoresist polymer commonly used in MEMS – was selected since the elastic structure of our VWNAV is made of this material. It was initially chosen because SU-8 and real insects wing veins show close mechanical properties [Bao et al., 2011].

The materials are compared using the two criteria and results are compiled in Table 1. The different values of the resonant criterion show that high yield steel and silicon are not particularly better suited for large amplitude vibrations than structural steel. For the yield criterion, as one could expect, using high yield steel enhances the performance and selecting a high yield silicon can be useful as well. Aluminium is a suitable choice that yields satisfactory results for both the resonant and the yield criteria. Overall, SU8 is a material that will enhance the large amplitude vibrations of a flexible structure as it is a better material than all the other classical materials in the comparison.

1.3. Nonlinear beam model: geometric nonlinearities

In the above sections, a linear model for the cantilever beam has been considered, valid for small displacements only. If the transverse displacement is increased, one has to consider geometrical nonlinearities. In the case of restrained ends in the axial direction, the geometrical nonlinearities come from an axial / bending coupling and a von Kármán model is enough, necessary if $w(x,t)$ is of the order of magnitude of the thickness h of the beam. In the present case of a cantilever beam, one has to consider higher-order models that take into account the effects of large rotations of the cross-section, necessary for higher transverse amplitude if $w(x,t)$ is of the order of magnitude of the length L of the beam (see e.g. [Lacarbonara and Yabuno, 2006; Thomas et al., 2016]). The dimensionless variables of Eqs. (2) have been chosen accordingly. We use here a so-called geometrically exact equation of motion of an inextensible cantilever beam in transverse motion, valid with no restriction on the rotation amplitude of the cross-sections of the beam [Thomas et al., 2016]:

$$\rho S \ddot{w} + EI \frac{\theta'''}{(\cos\theta)'} - \rho S \left(\tan\theta \int_L^x \ddot{u}\, \mathrm{d}x \right)' = p \tag{14}$$

with u the axial displacement, θ the rotation of the cross-section and other notations previously defined. Using the inextensionality constraints $(1+u')^2 + (w')^2 = 1$ and $\tan\theta = w'/(1+u')$, and expanding Eq. (14) in Taylor series truncated at order three in w, leads to:

$$EIw'''' + \rho S \ddot{w} + EI(w'w''^2 + w'^2 w''')' + \frac{\rho S}{2} \left[w' \int_L^x \frac{\partial^2}{\partial t^2} \left(\int_0^x w'^2 \mathrm{d}x \right) \mathrm{d}x \right]' = p, \tag{15}$$

which is the well-known model of a cantilever beam in nonlinear vibrations, first introduced in [Crespo da Silva and Glynn, 1978].

We consider the case of a base excitation. One can decompose the total displacement of a cross-section of the structure $w(x, t)$ as:

$$w(x, t) = w_e(t) + w_r(x, t), \tag{16}$$

where $w_e(t)$ is the base displacement and $w_r(x, t)$ is the relative displacement of the cross-section with respect to its base. Substituting Eq. (16) into Eq. (15) gives:

$$EIw_r'''' + \rho S\ddot{w}_r + EI(w_r' w_r''^2 + w_r'^2 w_r''')' + \frac{\rho S}{2}\left[w_r' \int_L^x \frac{\partial^2}{\partial t^2}\left(\int_0^x w_r'^2 \mathrm{d}x\right)\mathrm{d}x\right]' = -\rho S\ddot{w}_e. \tag{17}$$

Note that Eq. (17) is similar to Eq. (15) with $p = -\rho S\ddot{w}_e$. For a harmonic base excitation, it is possible to write the prescribed acceleration

$$\ddot{w}_e = \gamma_e \cos(2\pi f_e t), \tag{18}$$

with γ_e and f_e the amplitude and frequency of excitation. Using the dimensionless form presented in Eqs. (2), Eq. (17) becomes:

$$\bar{w}_r'''' + \ddot{\bar{w}}_r + (\bar{w}_r'\bar{w}_r''^2 + \bar{w}_r'^2\bar{w}_r''')' + \frac{1}{2}\left[\bar{w}_r' \int_1^{\bar{x}} \frac{\partial^2}{\partial \bar{t}^2}\left(\int_0^{\bar{x}} \bar{w}_r'^2 \mathrm{d}\bar{x}\right)\mathrm{d}\bar{x}\right]' = -\bar{\gamma}_e \cos(\Omega\bar{t}), \tag{19}$$

where

$$\bar{\gamma}_e = \gamma_e \frac{t_0^2}{L} = \gamma_e \frac{\rho S L^3}{EI}, \quad \Omega = \frac{2\pi f_e}{t_0} = \frac{2\pi f_e}{L^2}\sqrt{\frac{EI}{\rho S}}. \tag{20}$$

One can see that this is the linear equation of motion Eq. (3) appended with 2 nonlinear terms stemming from the geometrical nonlinearities. Then, expanding $\bar{w}_r(\bar{x}, \bar{t})$ onto the natural modes basis as in Eq. (9), substituting this equation into Eq. (19) and using the orthogonality properties of the modes, one obtains the following set of equations for the modal coordinates, for all $k \in \mathbb{N}^*$:

$$\ddot{q}_k + \omega_k^2 q_k + \sum_{i=1}^{+\infty}\sum_{j=1}^{+\infty}\sum_{l=1}^{+\infty}\left[\Gamma_{ijl}^k q_i q_j q_l + \Pi_{ijl}^k(\ddot{q}_j q_l + \dot{q}_j \dot{q}_l)q_i\right] = -\bar{\gamma}_e R_k \cos(\Omega\bar{t}), \tag{21}$$

with

$$R_k = \frac{\int_0^1 \Phi_k(\bar{x})\mathrm{d}\bar{x}}{\int_0^1 \Phi_k^2(\bar{x})\mathrm{d}\bar{x}}, \quad \Gamma_{ijl}^k = \frac{\int_0^1 \Phi_k\left(\Phi_i'\Phi_j''\Phi_l'' + \Phi_i'''\Phi_j'\Phi_l'\right)'\mathrm{d}\bar{x}}{\int_0^1 \Phi_k^2(\bar{x})\mathrm{d}\bar{x}}, \quad \Pi_{ijl}^k = \frac{\int_0^1 \Phi_k\left(\Phi_i'\int_1^{\bar{x}}(\int_0^{\bar{x}}\Phi_j'\Phi_l'\mathrm{d}\bar{x})\mathrm{d}\bar{x}\right)'\mathrm{d}\bar{x}}{\int_0^1 \Phi_k^2(\bar{x})\,\mathrm{d}\bar{x}}. \tag{22}$$

2. Nonlinear damping

2.1. Quadratic damping model

The nonlinear beam model introduced in the previous section is conservative. To take into account damping effects, we choose in this article to introduce damping terms directly in the modal oscillators Eq.(21). The main interest of using a modal damping model is that it can be easily experimentally identified, as it will be shown in the following. Since the identification procedure is based on a single resonance, we assume that it is possible to consider a single-mode response, valid for harmonic excitation, modes well separated in frequency and no internal resonances; consequently, Eqs. (21) are restricted to the k-th. oscillator only.

As in section 1.1, we first add a linear modal damping of factor ξ_k. We then add a supplementary quadratic modal damping term $\nu_k \dot{q}_k |\dot{q}_k|$ (with $|\bullet|$ the absolute value of $\bullet$), with coefficient ν_k, equivalent to a modal force proportional to the square of the velocity and always opposite to its direction. It stems

from an aeroelastic drag term, restricted to a single mode and thus neglecting the possible couplings with the others (see Appendix A). Even if higher order damping terms can be considered (see section 2.3), we restrict ourselves to the quadratic case since it will be shown in section 4 that this model is sufficient for the highly flexible structures considered in this article. Finally, omitting the k subscripts/superscripts for clarity purpose, Eq. (21) becomes:

$$\ddot{q} + 2\xi\omega_0\dot{q} + \nu\dot{q}|\dot{q}| + \omega_0^2 q + \Gamma q^3 + \Pi(\ddot{q}q^2 + \dot{q}^2 q) = -\bar{\gamma}_e R \cos(\Omega\bar{t}), \tag{23}$$

where

$$\Gamma = 8\int_0^1 \Phi'^2\Phi''^2\mathrm{d}\bar{x} \quad \Pi = 4\int_0^1 \left(\int_0^{\bar{x}} \Phi'^2(\bar{x})\mathrm{d}\bar{x}\right)^2 \mathrm{d}\bar{x}, \quad R = 4\int_0^1 \Phi(\bar{x})\mathrm{d}\bar{x}, \tag{24}$$

that can be calculated from Eqs. (22) with successive integration by parts (see for example [Arafat, 1999]) and because $\int_0^1 \Phi_k^2(\bar{x})\,\mathrm{d}\bar{x} = 1/4$ with the mode shape definition in Eq. (6). In Eq. (23), the ν parameter is modal, it may depend on the cross-section's width and the fluid mass density [Bidkar et al., 2009; Egorov et al., 2018].

The method of multiple scales [Nayfeh and Mook, 1979] [MS], limited to the first order, leads to a pure sine solution:

$$q(\bar{t}) = a \cos(\Omega\bar{t} - \phi). \tag{25}$$

The development of calculations covering this case and the one presented in subsection 2.3 is given in Appendix B. It shows that a and ϕ can be determined in the steady state with the system:

$$\begin{cases} \xi\omega_0 a + \eta\omega_0 a^2 &= -\dfrac{\bar{\gamma}_e R}{2\omega}\sin\phi \\ a\sigma - \dfrac{(3\Gamma - 2\omega_0^2\Pi)}{8\omega_0}a^3 &= \dfrac{\bar{\gamma}_e R}{2\omega}\cos\phi, \end{cases} \tag{26}$$

where $\eta = 4\nu/3\pi$ and $\sigma = \Omega - \omega_0$, the detuning parameter for a primary resonance. By eliminating ϕ between the two equations in Eq. (26), one can obtain the frequency response of the system near resonance [Malatkar and Nayfeh, 2003]:

$$\Omega - \omega_0 = \dfrac{(3\Gamma - 2\omega_0^2\Pi)}{8\omega_0}a^2 \pm \sqrt{\dfrac{(\bar{\gamma}_e R)^2}{4\omega_0^2 a^2} - \omega_0^2\left(\xi + \eta\, a\right)^2}. \tag{27}$$

With this model, valid only in the vicinity of a resonance, one can notice that the the effects of geometric nonlinearities – appearing in the first term with coefficients Γ and Π – and the damping – appearing in the second (square root) term – are independent. At the resonance point, the forcing energy and the damping loss offset each other, the term with the square root is zero and the first term gives the evolution of the frequency at resonance with respect to the amplitude a of the motion, which is here a quadratic relation. Then, the square root term in Eq. (27) includes an equivalent damping term:

$$\xi_{\mathrm{eq}} = \xi + \eta a. \tag{28}$$

Naturally, ξ is a dimensionless damping factor and thus its numerical value has a general meaning, independent of the structure and the mode considered. On the contrary, the quadratic term ηa is linear in the modal amplitude a of the motion. It thus depends on the mode shape scaling and more generally on the vibration amplitude scaling. For ξ_{eq} to be as general as ξ, the scaling must be defined accordingly. Referring to Eqs. (2), (9) and (25), the transverse displacement $w(x,t)$ and a are scaled with the characteristic length L of the structure, which leads to:

$$\xi_{\mathrm{eq}} = \xi + \dfrac{\eta}{\Phi_{\mathrm{max}}}\dfrac{w_{\mathrm{max}}}{L} = \xi + \hat{\eta}\dfrac{w_{\mathrm{max}}}{L}, \tag{29}$$

where w_{max} is the amplitude of the transverse motion of the structure where the deformed shape is maximum and $\Phi_{\text{max}} = \max_{\bar{x}} |\Phi(\bar{x})|$ is the corresponding value of the latter. The above equation shows that η depends on the mode shape scaling whereas $\hat{\eta} = \eta/\Phi_{\text{max}}$ does not. In this article, to confer a general meaning to the quadratic damping coefficient, we choose to use $\hat{\eta}$ (or η if the mode shapes are scaled such that $\Phi_{\text{max}} = 1$, which is the case for the mode shapes of Eq. (6)). As a consequence, the physical meaning of the quadratic damping coefficient $\hat{\eta}$ can be inferred as the equivalent modal damping factor when the maximum amplitude of vibration w_{max} of the structure is equal to the characteristic length L. Coefficient $\eta = 4\nu/3\pi$ has the same physical meaning, but is less general since it depends on the mode shape normalisation, as explained above.

2.2. Identification methods

Equation (27) leads to two methods to identify the damping coefficients ξ and $\hat{\eta}$ from the frequency domain: a classical half-power bandwidth identification of the equivalent damping, and a model-based identification technique, that is similar to what is proposed in [Krauss and Nayfeh, 1999].

2.2.1. Method 1 (M1): half-power bandwidth

In the case of a linear damping model, for small values of the damping factor ξ and well separated resonances, one can use the half-power bandwidth $\Delta\omega$ to identify ξ since $\xi \simeq \Delta\omega/(2\omega_0)$. Consequently, one can extend this method to estimate the equivalent damping factor ξ_{eq} for increasing values of the vibration amplitude, as long as the resonance frequency does not change much with the amplitude. For this, we measure the resonant response of the structure at a point of abscissa $\bar{x}_m$, for several input accelerations, and we estimate w_{res}, which is the amplitude, at resonance, of the displacement $w(\bar{x}_m, \bar{t})$. Then, with Eq. (9), $w_{\text{res}} = w_{\text{max}} \Phi(\bar{x}_m)/\Phi_{\text{max}}$ and for each resonance, ξ_{eq} can be written:

$$\xi_{\text{eq}} = \xi + c_0 w_{\text{res}}, \quad \text{and} \quad \hat{\eta} = L \frac{\Phi(\bar{x}_m)}{\Phi_{\text{max}}} c_0. \tag{30}$$

On the plot of ξ_{eq} as a function of w_{res}, the intercept and the slope give respectively the linear and quadratic modal damping coefficients $(\xi, \hat{\eta})$. This method will henceforth be referred to as "M1".

Besides, one can notice that the present identification method is independent of any structural model for the structure, since Eqs. (30) depend only on the characteristic length L of the structure and the relative amplitude of the deformed shape $\Phi(\bar{x})$ between the point where it is maximum and measurement point $\bar{x}_m$. In practice, one estimates ξ and c_0 with a linear fit of the experimental points $\xi_{\text{eq}} = f(w_{\text{res}})$ and deduces $\hat{\eta}$ with L and a measurement of the mode shape.

2.2.2. Method 2 (M2a, M2b): amplitude at resonance

At resonance, the forcing energy and the damping loss offset each other. In other words, the term under the square root in Eq. (27) vanishes, which gives an analytical relation between the amplitude at resonance a_{res}, the forcing amplitude and the damping:

$$\frac{\bar{\gamma}_e R}{2\omega_0^2} = \xi a_{\text{res}} + \eta a_{\text{res}}^2, \tag{31}$$

that leads to a single meaningful root (positive and strictly decreasing in ξ and η):

$$a_{\text{res}} = \sqrt{\left(\frac{\xi}{2\eta}\right)^2 + \frac{\bar{\gamma}_e R}{2\eta\omega_0^2}} - \frac{\xi}{2\eta}. \tag{32}$$

From Eq. (31), it is trivial to observe that for a linear modal damping model, the amplitude at resonance increases linearly with the forcing amplitude, whereas Eq. (32) demonstrates that when the quadratic damping coefficient is a non-zero value, the amplitude at resonance increases only with the square root of the forcing amplitude. In its dimensional form, Eq. (31) can be written:

$$\gamma_e = c_1 w_{\text{max}} + c_2 w_{\text{max}}^2, \tag{33}$$

with γ_e the prescribed base acceleration (see Eq. (18)), $w_{\max}$ defined in the previous section and with c_1 and c_2 two coefficients that can be extracted from measurements. By identifying Eq. (31) with Eq. (33) and using Eqs. (2), (8) and (20), one obtains:

$$\xi = \frac{R\Phi(\bar{x}_m)}{8\pi^2 f_k^2}\, c_1, \quad \text{and} \quad \hat{\eta} = \frac{R\Phi(\bar{x}_m)}{8\pi^2 f_k^2} L \frac{\Phi(\bar{x}_m)}{\Phi_{\max}} c_2, \tag{34}$$

with f_k the natural frequency of the considered mode of the structure (measured at low amplitude). One can notice that because $R\Phi(\bar{x}_m)$ (see Eq. (22)) does not depend on the mode shape normalisation, the same property logically holds for $(\xi, \hat{\eta})$. As a consequence, one has two alternatives for the identification.

First, if a structural model is known for the structure, one can calculate $\Phi(\bar{x}_m)$ and R from Eqs. (6) and Eq. (22) respectively. This leads to a model-based identification technique, which is henceforth referred to as "M2a", for which one has to measure the amplitude of the structure at a given point $\bar{x}_m$, at resonance, for several values of the input acceleration γ_e. Then, c_1 and c_2 are identified by a quadratic fit of the experimental points $\gamma_e = f(w_{\mathrm{res}})$ and Eq. (34) gives the value of $(\xi, \hat{\eta})$.

Second, if no structural model is available, estimating $\Phi(\bar{x}_m)$ and R experimentally is not straightforward. To overcome this difficulty, it is possible to first estimate ξ with a very low amplitude measurement (through method M1 for instance) and then use it to estimate $\hat{\eta}$ using the identified c_1 and c_2:

$$\hat{\eta} = \frac{c_2}{c_1} L \frac{\Phi(\bar{x}_m)}{\Phi_{\max}} \xi. \tag{35}$$

As in method M1, all quantities $(c_1, c_2, L, \Phi(\bar{x}_m)/\Phi_{\max})$ can be estimated through simple experiments. This method will be referred to as "M2b" from now on.

2.3. Higher order damping models

A number of nonlinear damping models exist in the literature, as presented in the introduction. To investigate their effects on the dynamics with relation to the quadratic model introduced in the previous section, two additional damping models are considered here. For this, Eq. (23) becomes:

$$\ddot{q} + 2\xi\omega_0\dot{q} + \omega_0^2 q + \nu_1\dot{q}|\dot{q}| + \nu_2\dot{q}^3 + \nu_3 q^2\dot{q} + \Gamma q^3 + \Pi(\ddot{q}q^2 + \dot{q}^2 q) = F\cos(\Omega\bar{t}). \tag{36}$$

It corresponds to the oscillator equation studied in the previous section, Eq. (23), with a generic dimensionless forcing F and two additional nonlinear damping terms, $\nu_2\dot{q}^3$ and $\nu_3\dot{q}q^2$. The former is introduced in [Gottlieb and Habib, 2012] in addition to the linear damping and aerodynamic drag damping to model the effect of air on a forced spherical pendulum. The latter models the viscoelasticity effects for plates in [Amabili, 2018a]. The forced response of the system in the steady state can be obtained with the method of multiple scales (cf. Appendix B) from:

$$\Omega - \omega_0 = \frac{(3\Gamma - 2\omega_0^2\Pi)}{8\omega_0} a^2 \pm \sqrt{\frac{F^2}{4\omega_0^2 a^2} - \omega_0^2 \left(\xi + \frac{4\nu_1}{3\pi}a + \left[\frac{3\omega_0\nu_2}{8} + \frac{\nu_3}{8\omega_0}\right]a^2\right)^2}; \tag{37}$$

in which the equivalent damping term is now:

$$\xi_{\mathrm{eq}} = \xi + \eta_1 a + (\eta_2 + \eta_3)a^2 \tag{38}$$

with $\eta_1 = 4\nu_1/(3\pi)$; $\eta_2 = 3\omega_0\nu_2/8$ and $\eta_3 = \nu_3/(8\omega_0)$.

One can notice that Eq. (37) can also be applied to a nonlinear mode of a non-symmetric structure with quadratic nonlinearities, such as a laminated plate or a shell with geometrical nonlinearities. In this case, $\Pi = 0$ and the sign of Γ gives the hardening / softening behaviour of the considered nonlinear mode. There is no need for an additional quadratic term in Eq. (36) since a normal form reduction, restricted to only one invariant nonlinear mode [Touzé et al., 2004; Denis et al., 2018]), shows that a single cubic term embeds the effects of all the non-resonant quadratic terms of the classical modal expansion.

As compared to the drag-like damping term associated to η_1, linear in a, the two additional damping terms linked to (η_2, η_3) are one order higher, quadratic in a. Moreover, it appears that for a given structure,

it seems difficult to distinguish the contributions in terms of damping of ν_2 or ν_3, since their effects are additive and appear at the same order. In the present study, those two additional higher order damping terms will not be considered since the experimental results (figures 5(c), 7(c), 8(c), 9(c,e)) show that the equivalent damping is well described by a linear function of a, with obviously no quadratic dependency. Consequently, the most pertinent damping term to include is $\nu_1|\dot{q}|\dot{q}$ for the tested structures of this article.

2.4. Numerical validation of the identification methods

In this section, we test the validity of the identification methods proposed in subsection 2.2. A linear oscillator and a Duffing oscillator – both appended with an aerodynamic drag damping term and both harmonically forced – are used to assess the methods' validity when applied to the numerical simulations of these oscillators. The former could model roughly the first mode of a cantilever beam as it is only slightly hardening. The latter is a simple model of more pronounced geometric nonlinearities effects. The reference numerical simulations are performed using the MANlab software [Cochelin et al., 2007; Lazarus and Thomas, 2010; Guillot et al., 2019], which combines periodic solution continuation with the harmonic balance method. More details have been postponed in Appendix C.

2.4.1. Linear oscillator with aerodynamic drag damping

The first oscillator tested is:

$$\ddot{q} + 2\xi\dot{q} + q + \nu\dot{q}|\dot{q}| = F\cos\left(\Omega\bar{t}\right). \tag{39}$$

The oscillator's nondimensional natural frequency has been set to 1; it would have been possible to reduce this equation to only 2 independent variables - (ξ, F) or (ξ, η) - by rescaling Eq. (39) in amplitude. This would have led to universal results, however, in order to simulate the beams tested experimentally, we chose to keep this formulation with these three coefficients. Indeed, since the damping depends on the vibration amplitude, the simulated frequency responses have (dimensionless) amplitudes in the range similar to that obtained experimentally, thanks to the tuning of the forcing amplitude.

To estimate the accuracy of our identification methods, we work on the simulated frequency responses of Eq. (39), plotted in dots (and captioned "MANlab") in Fig. 1(a) with the implemented values for the coefficients $(\xi, \hat{\eta}) = (0.001, 0.01)$, through $\nu = 3\pi\hat{\eta}/4$. The phase of the frequency responses is plotted in the graph of Appendix D. We use these frequency responses to test successively M1, M2a and M2b. First, following M1, we estimate ξ_{eq} using the half-power bandwidth method and plot it with yellow squares in Fig. 1(b), as a function of the amplitude at resonance a_{res}. This plot also shows with red circles the different values of ξ_{eq} computed with the implemented values $(\xi, \hat{\eta})$. Following Eq. (30), a linear fit gives $(\xi, \hat{\eta}) = (1.08\ 10^{-3}, 1.22\ 10^{-2})$ estimated by the M1 method. Whereas the value of ξ is well recovered, the value of $\hat{\eta}$ is slightly overestimated, which is qualitatively observed in Fig. 1(b) since the slopes of the two lines are different. Then, we also tested M2a and M2b by plotting F as a function of a_{res} (Fig. 1(c)) and estimating $(\xi, \hat{\eta}) = (1.05\ 10^{-3}, 0.99\ 10^{-2})$ and $(\xi, \hat{\eta}) = (1.08\ 10^{-3}, 1.02\ 10^{-2})$ respectively, with a quadratic fit (Eqs. (33), (34) and (35)). In this latter case, the identifications are much more precise.

Once these coefficients are obtained, one can reconstruct the frequency responses for the five different dimensionless forcing amplitudes (differentiated by colours) on Fig. 1(a). We use 2 different models for the reconstruction: a linear model ("Lin") for which we plot the modulus of the following complex function $1/(1 - \Omega^2 + 2i\xi_{\text{eq}}\Omega)$, with $\xi_{\text{eq}} = \xi + \hat{\eta}a_{\text{res}}$, and the MS model of Eq. (27). In both cases, the values of $(\xi, \hat{\eta})$ are those estimated with M1 and M2a. All resulting curves are plotted in Fig 1(a). The frequency responses using the M1-coefficients underestimate the amplitude at resonance (dotted and dashed lines), which is logical since the damping is overestimated, Fig 1(b). Furthermore a linear model using M2a-coefficients does not correlate exactly for high amplitude vibrations (solid lines) contrary to the multiple scales solution, that seems to fit quite well the numerical solution in the frequency range considered (dash-dotted lines).

Overall, this numerical analysis shows that the resonant amplitude-based method seems to be suited for the identification of our systems, and the multiple scales model is a good reconstruction method.

2.4.2. Duffing oscillator with aerodynamic drag damping

The structures of interest do not exhibit a significant nonlinear behaviour due to geometric nonlinearities when excited on their first mode (section 4). On other modes or structures with more pronounced geometrical
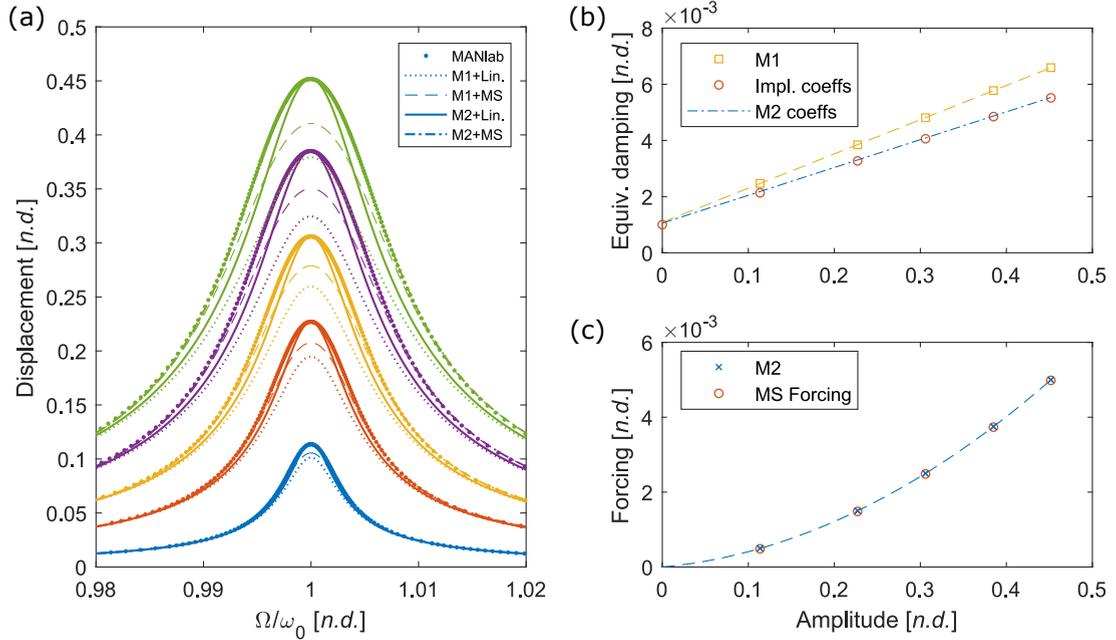
Figure 1: Validation of the identification methods, without geometric nonlinearities.
(a). Simulated and reconstructed frequency responses using M1 and M2 combined with a linear or a multiple scales model, (b). Illustration of M1 method, with identified ξ_{eq} values in squares and the fit (dashed line), to be compared with the ξ_{eq} values calculated with (i) the implemented coefficient values ($\xi=0.001$, $\hat{\eta}=0.01$) in circles and (ii) the coefficients identified using M2a (dash-dotted line), (c). Illustration of M2 method (crosses), with the MS Forcing calculated with Eq. (31) and implemented damping coefficients (circles).

nonlinearities, jump phenomena are observed in the frequency responses, which prevent the application of the half-power bandwidth method, thus making the damping identification more complex. It is possible to apply the method at very low amplitude and then use a linear model damping, but this method does not yield optimal results at large amplitude, as the response is overestimated. An example can be found in the experimental frequency responses shown in [Thomas et al., 2003, 2007] for plate and shell vibrations. The proposed identification method M2a may still be applied though, and its validity can be tested numerically. For this purpose, we consider the following oscillator which includes a cubic term:

$$\ddot{q} + 2\xi\dot{q} + q + \nu\dot{q}|\dot{q}| + \Gamma q^3 = F\cos(\Omega\bar{t}). \tag{40}$$

Re-scaling this equation can reduce the number of independent variables to 3.

The same process used for the oscillator of the previous section is applied here. The corresponding results are displayed on Fig. 2, with the same implemented damping coefficients $(\xi, \hat{\eta}) = (0.001, 0.01)$ and with $\Gamma=-1$. These simulations show that the method is still relevant for structures displaying geometric nonlinearities effects, although the equivalent damping reconstructed with the identified coefficients (dash-dotted line, with $(\xi, \hat{\eta})=(1.7\ 10^{-3}, 6.8\ 10^{-3})$) does not match as well the equivalent damping calculated with the implemented coefficients (solid line) Fig 2(b). Indeed, using the identified coefficients on the reconstructed frequency responses (M2a+MS) yields good results at high amplitude Fig 2(a). On the other hand reconstruction using the MS model with the implemented coefficients is accurate for amplitudes up to $0.3a$, but underestimates the amplitude beyond that. Overall, the reconstructions with the identified coefficients fit better to the "real" solutions. This standout result is due to the fact that Eq. (31) is not accurate for high amplitudes, see Fig. 2.(c), which is directly related to the validity limit of first order approximation in the multiple scales
.

In addition, MANlab also gives the amplitude of the other harmonics of the solution. In accordance with the theory and the multiple scales development (see Appendix B), the amplitudes of the constant value and the second harmonic of the solution are *de facto* null (5 orders of magnitude lower, near the float resolution).
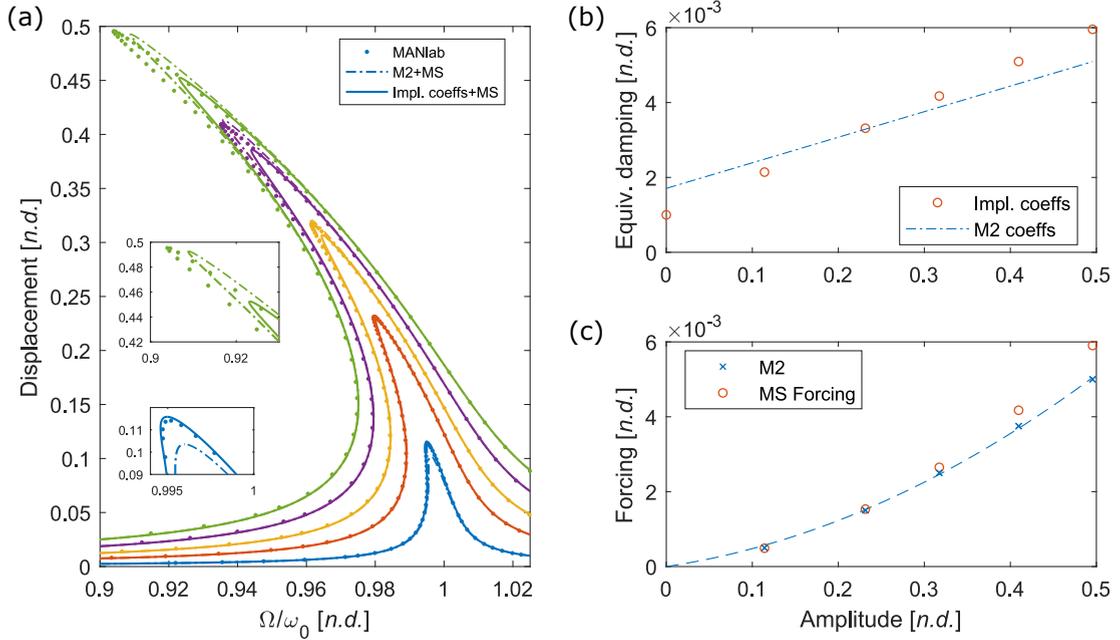
Figure 2: Validation of the second identification method, with geometric nonlinearities.
(a) Simulated frequency responses with $\Gamma=-1$, superimposed with the frequency responses reconstructed with the damping coefficients identified using M2a or directly the implemented coefficients ($\xi=0.001$, $\hat{\eta}=0.01$), (b). Comparison of the ξ_{eq} obtained with M2 and the implemented values, (c). Illustration of M2 (crosses), with the forcing calculated with Eq. (31) and the implemented damping coefficients (circles).

The plot is not reproduced here for synthesis purpose. For the oscillator of the previous section, the third harmonic amplitude was also limited; whereas the amplitude of Eq. (40) solution's third harmonic is more and more important as the forcing increases, due to the geometric nonlinearities. This may explain the various degrees of accuracy of the MS model, as the approximation of a solution in the form of a pure sine function is verified or not.

However, the correlation for these reconstructions is in much better agreement than a strictly linear damping model, for the values of the damping coefficients that were chosen in the range obtained experimentally. Indeed, for such a model, the amplitude at resonance is inversely proportional to the damping, and since the equivalent damping at high amplitude is around five times the damping at low amplitude Fig. 2.(b), this would lead here to an overestimation of the response at high amplitude by a factor 5.

3. Experimental setup

The identification techniques proposed in subsection 2.2 are used to identify the damping coefficients of several structures, presented in subsection 3.1. The whole measurement process is described in subsection 3.2.

3.1. Specimens

The different structures tested are presented in Fig. 3. A photograph of the maximum amplitude obtained is presented as well when it is significant.

The first structure tested is a steel ruler, as it is readily available and easy to measure, which allows validating the identification method and the set-up. Figure 3(a) displays the ruler clamped at the desired length, set on the shaker, ready for the measurement, with an accelerometer at its base and a vibrometer targeting the measuring point. Figure 3(b) shows the beam vibrating in profile. The trace is in light green and the maximum positions of the beam are highlighted. The second tested structure is a micro beam, hereinafter referred to as μ-beam, made of SU-8 polymer (Figs. 3(c,d)). It has a comparable width-to-thickness ratio with the steel ruler. Its testing helps determining the influence of material and scale on
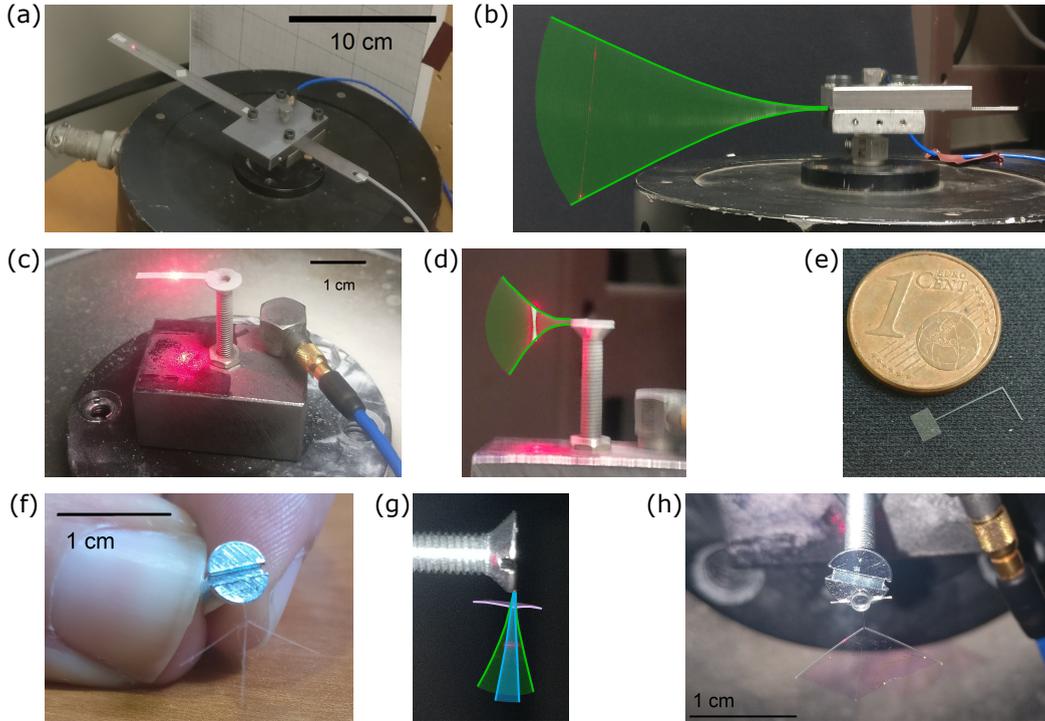
Figure 3: Photographs of tested specimens.
(a). Steel ruler at rest, (b). Maximum amplitude obtained for steel ruler, (c). μ-beam at rest, (d). Maximum amplitude obtained for the μ-beam, (e). L-beam at rest, (f). WS (Wing skeleton) at rest, (g). Maximum amplitude obtained for WS, (h). Wing at rest.

damping. A similar set-up is used, however, for the present μ-beam and all the other micro-structures introduced below, the clamping is made by gluing them on a flat surface: the head of a given countersunk screw that has a first axial mode much higher than the frequency range of interest.

The other tested structures are micro-scale beam assemblies which are ever more looking alike a wing of our VWNAV. The first beam assembly tested is the simplest possible: it is 2 beams which are assembled perpendicularly (the resulting "L" shape justifies the notation L-beam). Figure 3(e) presents the L-beam (and its gluing surface) and an adjacent 1-cent coin, which serves as a scale. The second beam assembly tested is a structure resembling our VWNAV, but without membrane [Faux et al., 2018]. By testing this structure and a "real" VWNAV wing, it is possible to estimate the contribution to damping of the membrane. This "wing skeleton" structure (shortened to "WS") is presented on Figs 3(f,g). Each trace of its beams is coloured in light blue, green and pink respectively, and the maximum positions of each beam are again highlighted. The last tested structure is a wing (or simply W), sampled from an existing prototype. Its characterisation can serve the design of future prototypes. Fig. 3(h) presents the wing set on the shaker.

The main geometric parameters are detailed in Table 2. The recurring characteristic length of 8 millimetres has been chosen specifically for comparison purposes with the VWNAV wing, as well as the cross-sections' geometry.

## 3.2. Measurement process and materials
3.2.1. Experimental set-up

A stepped-sine experiment is performed with the set-up presented in Fig. 4. The excitation amplitude is set to a given value of acceleration that is maintained constant throughout the measurement to establish a frequency response. The computer generates a signal that a digital-to-analogue converter (DAC) feeds to a power amplifier to activate an electromagnetic shaker (Brüel & Kjær 4808). The base acceleration is measured with an accelerometer and is looped back into a controller to counter the interaction of the

Structure	L	h	b
Steel ruler	130	0.5	1.3
μ-beam	12	0.08	1.6
L-beam	8	0.08	0.08
WS	8	0.08	0.08
Wing	8	0.08	0.08

Table 2
Characteristic geometric parameters of the tested structures (Length L, thickness h and width b, in millimetres).
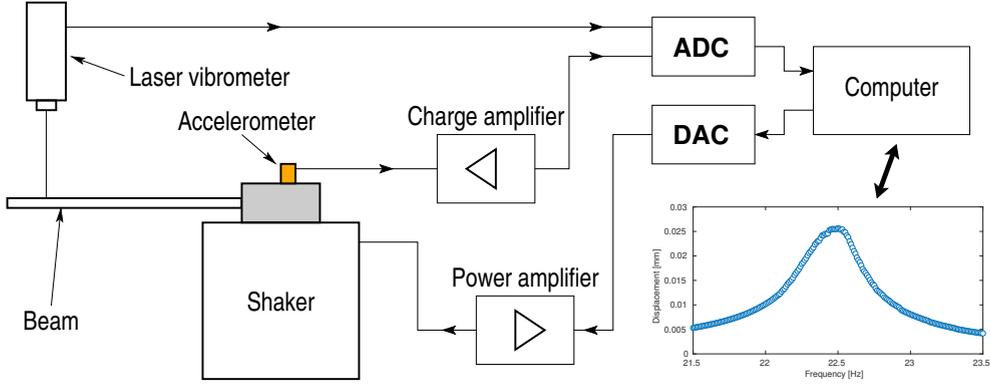
Figure 4: Experimental setup for the measurement of the frequency response curves.

structure with the shaker, avoiding force drops off near resonance [Varoto and de Oliveira, 2002]. The displacement of the beam is measured with a laser Doppler vibrometer (Polytec PSV400 scanning laser vibrometer). Thanks to an ad-hoc lense system, the laser beam focus can be made compatible with the structure's small geometry; one can see the laser spot in Figs. 3(a,c,d). The amplitudes of the first harmonics of the beam's velocity and base acceleration signals are then extracted using a homodyne detection in the steady state. Then the relative displacement can be calculated and plotted for each tested frequency.

3.2.2. Homodyne detection
Let $s(t)$ be a given periodic time signal, that one can write $s(t) = s_0 + \sum_{k=1}^{N} a_k \sin(k\omega t + \phi_k)$. We are searching for a_1 and ϕ_1, the amplitude and phase of the first harmonic of that signal (the calculation may be applied to any harmonic). We first multiply $s(t)$ by a cosine and a sine function at the frequency of the first harmonic: $s_c(t) = s(t)\cos(\omega t)$, $s_s(t) = s(t)\sin(\omega t)$. By calculating the mean of each product $\langle s_c(t) \rangle$ and $\langle s_s(t) \rangle$, one can show that $\langle s_c(t) \rangle \approx \sin(\phi_1) a_1/2$, $\langle s_s(t) \rangle \approx \cos(\phi_1) a_1/2$, if the duration T of the mean is large compared to the largest time period of the signal (i.e. $T \gg 2\pi/\omega$), and the phase is not random. Amplitude and phase are then:

$$a_1 \approx 2\sqrt{\langle s_c(t) \rangle^2 + \langle s_s(t) \rangle^2} \quad \text{and} \quad \phi_1 \approx \arctan\left(\frac{\langle s_c(t) \rangle}{\langle s_s(t) \rangle}\right). \tag{41}$$

3.2.3. Relative displacement calculation
The displacement w_r is obtained by subtracting the displacement of the base w_e to the total displacement w, according to Eq. (16). Using the homodyne detection (3.2.2) for the first harmonics of the vibrometer signal and the accelerometer signal (respectively noted $v_{\text{vib}}(t) = V\cos(2\pi f_e t + \psi_v)$ and $a_e(t) = \gamma_e \cos(2\pi f_e t + \psi_a)$) and then integrating them gives:

$$w(t) = \frac{V}{2\pi f_e}\cos(2\pi f_e t + \psi_v - \pi/2), \quad \text{and} \quad w_e(t) = \frac{\gamma_e}{(2\pi f_e)^2}\cos(2\pi f_e t + \psi_a - \pi). \tag{42}$$

Denoting by W and α the amplitude and phase of the first harmonic of the seeked relative displacement

and applying Eq. (41) yields:

$$W = \frac{1}{2\pi f_e} \sqrt{V^2 + \frac{\gamma_e^2}{4\pi^2 f_e^2} - \frac{V\gamma_e}{\pi f_e} \cos\left(\psi_v - \psi_a + \pi/2\right)}$$

$$\alpha = \arctan \frac{2\pi V f_e \sin\left(\psi_v - \pi/2\right) - \gamma_e \sin\left(\psi_a - \pi\right)}{2\pi V f_e \cos\left(\psi_v - \pi/2\right) - \gamma_e \cos\left(\psi_a - \pi\right)}.$$

(43)

This process is crucial as the beam total displacement is not measured at the tip to limit the effect of axial displacement at very large transverse amplitude. Therefore, it presents an antiresonance that is marked increasingly with a decreasing abscissa along the beam's length.

3.2.4. Data processing for identification and reconstruction

A synoptic description of the data processing is the following:

1. Plot the frequency response of the relative displacement for all tested acceleration amplitudes
2. Plot γ_e as a function of maximum amplitude $w_{\max}$
3. Extract the polynomial coefficients of the fitting curve
4. Extract ξ and $\hat{\eta}$, either using
   - Eq. (34), i.e. M2a
   - M1 to identify ξ, and Eq. (35) to extract $\hat{\eta}$, i.e. M2b
5. Reconstruction of the frequency responses either using
   - the MS model
   - the linear model

4. Experimental results

For all tested structures, the materials properties were determined individually. With the mass of the samples (obtained with a precise balance) and their volume (calculated), one can calculate the density ρ: for the ruler's steel and SU-8, it led to $\rho_S = 7920$ kg.m^{-3} and $\rho_{SU-8} = 1290$ kg.m^{-3} respectively. Assuming a perfect clamped boundary condition gives Eq. (8) for the natural frequencies. By adjusting the slope of the theoretical versus analytical frequencies of the first four modes of the cantilever beams, we find the Young's modulus of the tested beam experimentally (we also assume it does not vary between the different fabricated structures). The identified values of Young moduli are included in Table 1. Besides, for all experimental frequency responses processing, a smoothing filter was used to minimise the impact of artefacts of measurements on the identification. The filter used is the Savitzky-Golay algorithm, (Matlab *sgolayfilt* function from the Signal Processing Toolbox). The only plot displaying filtered data is the comparison of the identification methods and reconstruction models on experimental frequency responses (Fig. 6), and mentions it explicitly in the caption: -(filt). As explained in section 2, since the values of the identified coefficients c_1 and c_2 depend on the scaling, they are not given in this paper. However the identified values of ξ and $\hat{\eta}$ (directly related to c_1 and c_2) are detailed in Table 3 for all tested structures.

4.1. Cantilever beams

Figure 5 presents the identification for the macroscale steel ruler of Figs. 3(a,b). Very large amplitudes have been tested, up to 0.3 times the length of the beam, more than half of it for the peak-to-peak amplitude. A few of the measured frequency responses near the first mode are plotted in Figs. 5.(a,b). The hardening behaviour predicted analytically is perceptible, but not significant. Furthermore, if the damping was linear, the phase would be independent of the forcing amplitude. In Fig. 5.(b), the phase variation at the vicinity of the resonance is reduced – it becomes more and more "flat" – as the forcing increases. This effect is also observable in Appendix D, with the plot of the amplitude and the phase of the simulated frequency responses. This effect was noticed in the study [Ramananarivo et al., 2011] as well. Figs 5.(c,d) show the fits for the two identification methods M1 and M2a. Both can be well described by a linear or quadratic function of a, depending on the method used.
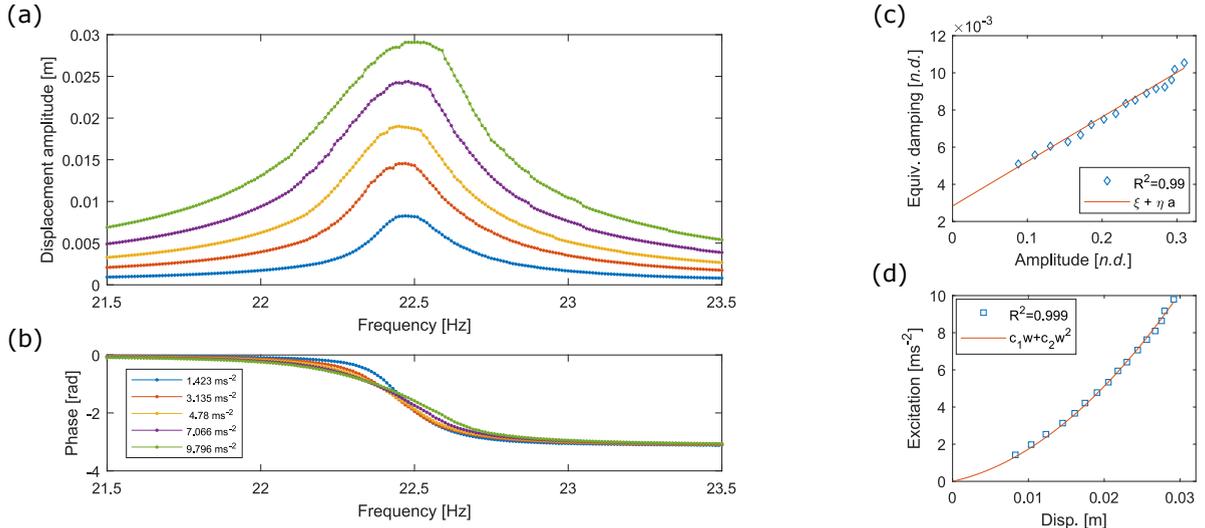
Figure 5: Damping coefficients extraction for the ruler's first mode.
(a). Measured frequency responses, (b). Measured phase of the frequency responses, (c). Illustration of M1 applied to the ruler, (d). Illustration of M2a applied to the ruler. R^2 gives the coefficient of determination to confirm the fit.
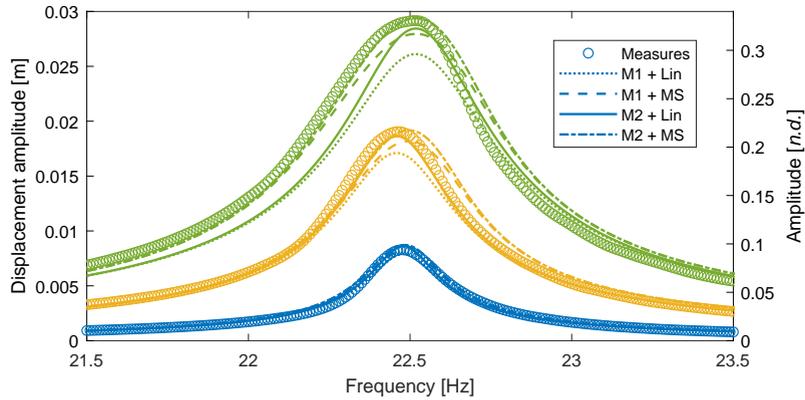

Figure 6: Experimental validation of identification methods and models for a steel ruler-(filt).

Figure 6 is analogous to Fig. 1 with data from experiments, i.e. the different identification methods and reconstruction models are compared on experimental data. Similar observations can be made on the identification techniques: the half-power bandwidth method M1 combined with a linear model does not yield the best correlation, whereas the combination of the second identification technique M2a (or M2b) and the multiple scales model should be the preferred method.

Figures 7(a,b) display the frequency responses in the vicinity of the first mode of the micro beam shown on Figs. 3(c,d). Very large amplitudes were obtained, with the maximum dimensionless amplitude around 0.4 times the length of the beam, which corresponds to 80% in peak-to-peak amplitude. Figs. 7(c,d) illustrate the identification methods 1 and 2 respectively. As M1's accuracy depends on the quality of the frequency response, and the last two frequency responses function present higher experimental error, only the four first points were used for the fit. One can verify that the last two points do not represent a change in the damping behaviour by examining the results of M2 in Fig. 7(d). The reconstructed frequency responses (Fig. 7a) use the second identification method (M2a) and the multiple scales model. The correlation is satisfactory up to very high amplitudes.
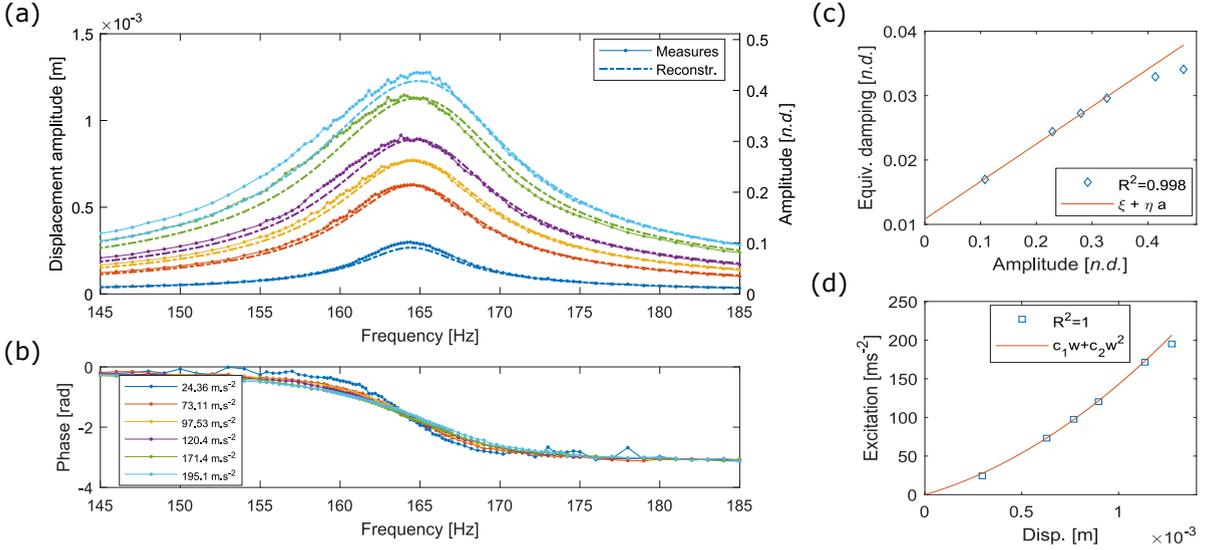
Figure 7: Measurement, identification and reconstruction for μ-beam (mode 1).
(a). Measured and reconstructed frequency responses in both dimensional and dimensionless scales, (b). Measured phase of the frequency responses, (c). M1 illustration, (d). M2 illustration

4.2. Beam assemblies

This section addresses the vibratory response of the beam assemblies shown on Figs. 3(e,f,g,h). As explained in section 2.2.2, we need a structural model to apply M2a identification. Since, as it will be shown, the frequency responses of those structures do not show any hardening or softening behaviour, a linear structural model should be accurate enough (Fig. 1.(a)), as the one presented in [Faux et al., 2019]. Some discrepancies in the natural frequencies where observed between the measured ones and the ones from the model, attributed to unavoidable imperfections in the geometry and the boundary conditions. Therefore, we prefer here to use the M2b identification method, which does not need any structural model of the structure.

Besides, the L-beam and the wing skeleton displayed in-plane vibrations that caused a loss of focus of the vibrometer, thus preventing measurements at large amplitude. This explains the weak maximum measured amplitude obtained on the graphs when compared to the photograph Fig 3.(g). This may be related to the choice of a square cross-section for these structures [Pai and Nayfeh, 1990].

We first consider the L-shaped beam of Fig. 3(e), with the main beam of length 8 millimetres and the perpendicular segment of 4 millimetres. The measured and reconstructed frequency responses are displayed on Figs. 8(a,b), with the identifications illustrated in Figs. 8(c,d). Again, it is shown that the proposed identification method allows to obtain a good correlation between the measured and reconstructed curves which validates its use for the case of single-mode responses of beam assemblies.

Then, we consider the wing skeleton and NAV wing of Figs. 3(f,g,h). As compared to the previous structures, these have been designed to have the first two modes very close in frequency [Faux et al., 2018], which is clearly seen on the frequency responses, Figs. 9-10(a). Therefore, the structural response at frequencies between the two natural frequencies includes the contribution of both modes due to the frequency closeness of the modes, which invalidates the single-mode hypothesis of the damping model proposed here. To circumvent this problem, it could be possible to perform a study of the interaction between these degrees of freedom, but this is out of the scope of this article, as deriving a multi-mode model including a quadratic damping coupling is not straightforward, mainly because of the non-direct modal expansion of the velocity modulus (see Appendix A). For these structures, the identification methods have been tested separately on the two resonances considering two separate oscillators. In the immediate vicinity of both resonances, the reconstructed frequency responses of the WS and NAV wing match quite well the measured
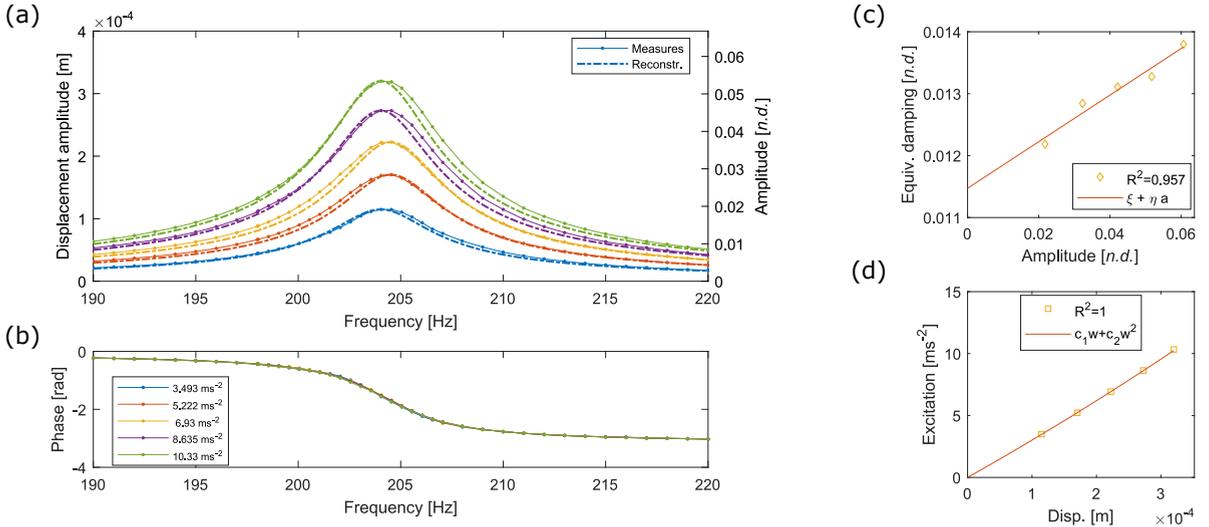
Figure 8: Measurement, identification and reconstruction for L-beam (mode 1).
(a). Measured and reconstructed frequency responses in both dimensional and dimensionless scales, (b). Measured phase of the frequency responses, (c). M1 illustration, (d). M2 illustration.
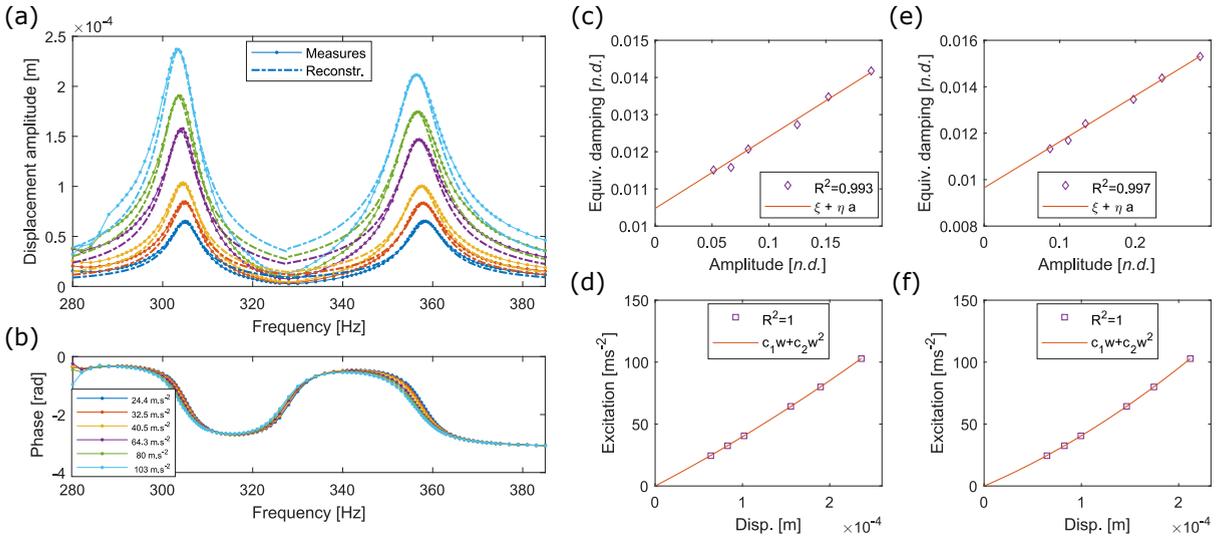

Figure 9: Measurement, identification and reconstruction for the Wing skeleton (bending and twisting modes).
(a). Measured and reconstructed frequency responses in the vicinity of both modes, (b). Measured phase of the frequency responses, (c). M1 on twisting mode, (d). M2 on twisting mode, (e). M1 on bending mode, (f). M2 on bending mode.

frequency responses, which would indicate that the damping coefficients are well captured and the single-mode approximation holds at resonance. In addition, the effect of nonlinear damping may be seen clearly on Figs. 9(b,f).

Last, for the specific case of the wing removed from a prototype of our VWNAV, one may notice that the two resonances appear for frequencies lower than in the case of the wing skeleton. This may be due to the added mass effect of the surrounding fluid. For the first mode, the first point has been discarded from the fit to improve its quality. The apparent overestimation of the damping for this point may be related to
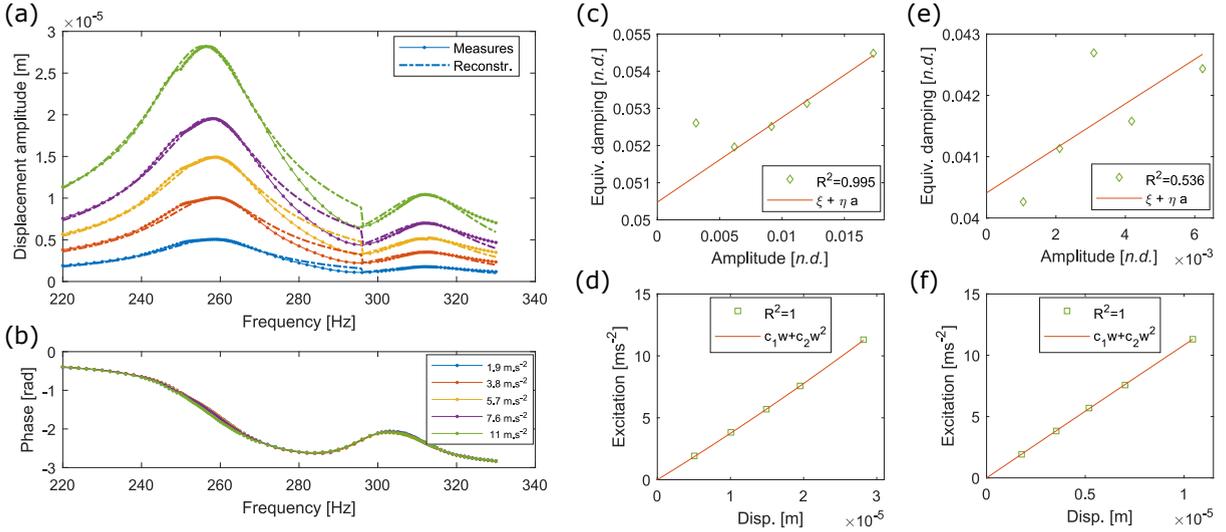
Figure 10: Measurement, identification and reconstruction for the "true" wing (bending and twisting modes).
(a). Measured and reconstructed frequency responses in the vicinity of both modes, (b). Measured phase of the frequency responses, (c). M1 on bending mode, (d). M2 on bending mode, (e). M1 on twisting mode, (f). M2 on twisting mode.

the modal combination. Indeed, at low amplitude, the half-power bandwidth of a mode may be impacted by the other mode. For higher amplitudes, this can still be true for the second mode as its peak is lower. Since Eq. (35) uses the linear damping coefficient identified with the half-power bandwidth method, which does not yield good results here (Fig 10(c,e)), the validity of the damping coefficients identified is not guaranteed. Moreover, the quadratic damping coefficient of the twisting mode was found negative – the displacement amplitude range is very limited, which reduces the significance of the identification. The addition of the membrane strengthens the coupling of the structure with the fluid, which increases the nonlinear coupling between the modes and renders the assumption of single-mode response less valid.

4.3. Damping comparison

The measurements led to the identification of various damping coefficients. Figure 11 presents the equivalent damping ξ_{eq} reconstructed with Eq. (29) and the identified $(\xi, \hat{\eta})$ coefficients, for the various tested structures, on the amplitude range tested. The first conclusion to be drawn is that the SU-8 structures have a higher linear modal damping than the steel ruler. It may be related to the viscoelasticity of the material. Furthermore, one can notice that the structures with larger widths (the cantilevers) have higher aerodynamic damping which is consistent with the aerodynamic force parameters [Bidkar et al., 2009]. The quadratic damping coefficient is also smaller for the wing skeleton's twisting mode than for the bending mode, which would indicate a priori a lower lift generation for the twisting mode. For weakly damped structures, taking into account a quadratic damping term allows a better correlation, as the equivalent damping varies in the range of tested amplitudes. In the case of the L-beam and the NAV wing second mode, the phase plots (Figs. 8,10(b)) do not display a significant dependence on the excitation amplitude, which could be interpreted as a low quadratic damping (with the converse reasoning of section 4.1). Hence a linear damping model could be sufficient.

As explained in the previous section, the identification method for the drone wing gives low confidence values. This said, the linear damping coefficient values are localised around 0.04-0.05. It is interesting to note that it is around five times higher than the coefficient in absence of membrane, which was unexpected as the effect of the membrane was believed to increase the quadratic damping coefficient only. It could be due to the limit of the identification method, however the membrane does have an effect even for very small amplitude vibrations, which correspond to the Stokes regime (Re<1), (in which the action of air on the structure is taken into account with a Stokes drag that depends linearly on the velocity [Stokes, 1851]).

Structure	Macro	μ-beam	L-beam	WS,b	WS,t	W,b	W,t
ξ %	0.26	1.22	1.15	0.78	1.05	5.05*	4.32*
$\hat{\eta}$ %	2.20	3.24	0.80	1.23	1.00	30.6*	*
Re ($L_c = b$)	2.8 10^3	3.1 10^2	2.01	14.6	11.5	0.85	0.31

Table 3
Damping coefficients and Reynolds numbers at maximum measured amplitude for the different modes of the tested structure. (* Damping coefficient values of W have a low confidence)
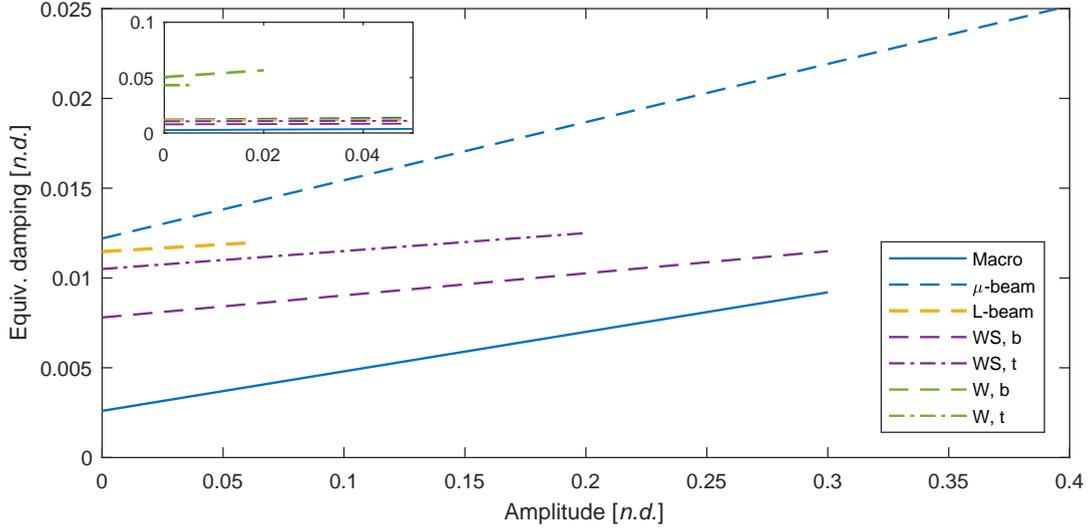

Figure 11: Reconstructed equivalent damping ξ_{eq}, computed with the values identified using M2a (cantilever beams) and M2b (beam assemblies) for the tested modes.

In this regime, the action of air on the structure is then easily translatable into a linear modal damping. Therefore an increase in the linear damping factor may not be absurd.

Conclusion

In this article, we investigated several aspects of a nonlinear quadratic damping term, due to fluid structure interactions, and its application to the large amplitude vibrations of cantilever highly flexible structures. An initial result was that such a model can be viewed in a certain sense as a classical linear damping model with an equivalent damping coefficient that depends linearly on the amplitude of motion. In order to confer a general meaning to this quadratic damping coefficient, special care was taken to make it dimensionless, so that its influence on the dynamics can be compared from one structure to another one, as it is usually done with a linear damping ratio. It was also demonstrated, in the case of the considered structures, that this model was both necessary – since the equivalent damping values vary significantly in the range of tested amplitudes – and sufficient compared to other nonlinear damping models – as the experimental equivalent damping is well described by a line function of the displacement amplitude.

We also proposed and tested original identification techniques for experimental estimation of the linear and quadratic modal damping coefficients. These techniques are applicable to single-mode responses only, therefore for structures with a weak fluid-structure interaction. A first technique is based on the linear damping model; it uses the half-power bandwidth method to identify the two damping coefficients. The model gives rise to another original technique that is based on the measurement of the amplitude at resonance of the considered mode, for several amplitudes of excitation in the steady state. Two versions were presented: (a) a fully analytical version that uses the structural model, and that has the advantages of being self-sufficient and applicable to structures displaying geometric nonlinearities, and (b) a hybrid version that uses

the half-power bandwidth method to determine the linear modal damping factor. These techniques were validated numerically thanks to simulations in the frequency domain as well as with several experimental tests, showing that one of them has a better accuracy. Because our identification technique is based on the measurement of the system nonlinear frequency response in the vicinity of a given resonance, recent experimental continuation techniques (see [Denis et al., 2018] and reference therein) could be more convenient than the stepped sine experiments used in the present study. Their investigation is left for further studies.

Finally, our quadratic air flow model was theoretically compared to other nonlinear damping models of the literature – all cubic – showing that in the case of a complete model, the equivalent damping ratio was a quadratic function of the vibration amplitude. In our experiments, it was shown that the quadratic order was the leading one, since the damping ratio was found linear with respect to the amplitude, demonstrating that our fluid structure damping was predominant over other sources of damping. This was probably due to the cantilever boundary conditions of our structures, which favours their high flexibility and thus very high amplitude displacements for low driving forces. For more constrained structures such as plates and shells, the classical bending / membrane coupling gives rise to geometrical nonlinearities for lower amplitudes of displacement and viscoelastic effects have been identified as the main source of nonlinear damping, with a damping term most of the time identified as cubic (see Fig. 7 of Amabili [2018a] and Amabili [2018b, 2019]). It could be interesting to study and identify on such structures both a quadratic – aeroelastic drag like model – in addition to the viscoelastic one, to experimentally verify the contribution of both effects, confirm and explain the predominance of a viscoelastic cubic damping. This is left for further studies.

Acknowledgments

References

Alijani, F., Amabili, M., Balasubramanian, P., Carra, S., Ferrari, G., Garziera, R., 2016. Damping for large-amplitude vibrations of plates and curved panels, Part 1: Modeling and experiments. International Journal of Non-Linear Mechanics 85, 23–40. URL: https://linkinghub.elsevier.com/retrieve/pii/S0020746216300415, doi:10.1016/j.ijnonlinmec.2016.05.003.

Amabili, M., 2018a. Nonlinear damping in large-amplitude vibrations: modelling and experiments. Nonlinear Dynamics 93, 5–18. URL: http://link.springer.com/10.1007/s11071-017-3889-z, doi:10.1007/s11071-017-3889-z.

Amabili, M., 2018b. Nonlinear damping in nonlinear vibrations of rectangular plates: Derivation from viscoelasticity and experimental validation. Journal of the Mechanics and Physics of Solids 118, 275–292. URL: https://linkinghub.elsevier.com/retrieve/pii/S0022509618303363, doi:10.1016/j.jmps.2018.06.004.

Amabili, M., 2019. Derivation of nonlinear damping from viscoelasticity in case of nonlinear vibrations. Nonlinear Dynamics 97, 1785–1797. URL: http://link.springer.com/10.1007/s11071-018-4312-0, doi:10.1007/s11071-018-4312-0.

Amabili, M., Alijani, F., Delannoy, J., 2016. Damping for large-amplitude vibrations of plates and curved panels, part 2: Identification and comparisons. International Journal of Non-Linear Mechanics 85, 226–240. URL: https://linkinghub.elsevier.com/retrieve/pii/S0020746216300427, doi:10.1016/j.ijnonlinmec.2016.05.004.

Anderson, T.J., Nayfeh, A.H., Balachandran, B., 1996. Experimental Verification of the Importance of the Nonlinear Curvature in the Response of a Cantilever Beam. Journal of Vibration and Acoustics , 7.

Ansari, S.A., Knowles, K., Żbikowski, R., 2006. A nonlinear unsteady aerodynamic model for insect-like flapping wings in the hover: Part I. Methodology and analysis. Journal of Aerospace Engineering 220, 61–83.

Arafat, H.N., 1999. Nonlinear Response of Cantilever Beams. Ph.D. thesis. Virginia Tech.

Aureli, M., Porfiri, M., 2010. Low frequency and large amplitude oscillations of cantilevers in viscous fluids. Applied Physics Letters 96, 164102. URL: http://aip.scitation.org/doi/10.1063/1.3405720, doi:10.1063/1.3405720.

Balasubramanian, P., Ferrari, G., Amabili, M., 2018. Identification of the viscoelastic response and nonlinear damping of a rubber plate in nonlinear vibration regime. Mechanical Systems and Signal Processing 111, 376–398. URL: https://linkinghub.elsevier.com/retrieve/pii/S0888327018301882, doi:10.1016/j.ymssp.2018.03.061.

Bao, X., Bontemps, A., Grondel, S., Cattan, E., 2011. Design and fabrication of insect-inspired composite wings for MAV application using MEMS technology. Journal of Micromechanics and Microengineering 21, 125020. URL: http://stacks.iop.org/0960-1317/21/i=12/a=125020?key=crossref.139bf5b6fe2a0f7ac8246168aaf311f8, doi:10.1088/0960-1317/21/12/125020.

Bidkar, R.A., Kimber, M., Raman, A., Bajaj, A.K., Garimella, S.V., 2009. Nonlinear aerodynamic damping of sharp-edged flexible beams oscillating at low Keulegan Carpenter numbers. Journal of Fluid Mechanics 634, 269. URL: http://www.journals.cambridge.org/abstract_S0022112009007228, doi:10.1017/S0022112009007228.

Bikdash, M., Balachandran, B., Nayfeh, A.H., 1993. Melnikov analysis for a ship with a general roll-damping model. Nonlinear Dynamics 6, 101–124.

Bontemps, A., Vanneste, T., Paquet, J.B., Dietsch, T., Grondel, S., Cattan, E., 2013. Design and performance of an insect-inspired nano air vehicle. Smart Materials and Structures 22, 014008. URL: http://stacks.iop.org/0964-1726/22/i=1/a=014008?key=crossref.e0373f1dea6daf02a8a85b77e8fd67ab, doi:10.1088/0964-1726/22/1/014008.

Cadot, O., Ducceschi, M., Humbert, T., Miquel, B., Mordant, N., Josserand, C., Touzé, C., 2016. Wave Turbulence in Vibrating Plates, in: Skiadas, C.H., Skiadas, C. (Eds.), Handbook of Applications of Chaos Theory. 1 ed.. Chapman and Hall/CRC, Boca Ration : Taylor & Francis, 2016.|"A CRC title.", pp. 425–448. URL: https://www.taylorfrancis.com/books/9781466590441/chapters/10.1201/b20232-21, doi:10.1201/b20232-21.

Chaigne, A., Lambourg, C., 2001. Time-domain simulation of damped impacted plates. I. Theory and experiments. The Journal of the Acoustical Society of America 109, 1422–1432. URL: http://scitation.aip.org/content/asa/journal/jasa/109/4/10.1121/1.1354200, doi:10.1121/1.1354200.

Chouvion, B., McWilliam, S., Popov, A.A., Fox, C.H.J., 2012. Review and comparison of different support loss models for micro-electro-mechanical systems resonators undergoing in-plane vibration. Proceedings of the Institution of Mechanical Engineers, Part C: Journal of Mechanical Engineering Science 226, 283–295. URL: http://journals.sagepub.com/doi/10.1177/0954406211413351, doi:10.1177/0954406211413351.

Cochelin, B., Damil, N., Potier-Ferry, M., 2007. Méthode asymptotique numérique. Hermes Lavoisier. URL: https://hal.archives-ouvertes.fr/hal-00487343.

Dalzell, J.F., 1976. A note on the form of ship roll damping. Technical Report SIT-DL-76-1887. Sevens Institute of Technology.

Denis, V., Jossic, M., Giraud-Audine, C., Chomette, B., Renault, A., Thomas, O., 2018. Identification of nonlinear modes using phase-locked-loop experimental continuation and normal form. Mechanical Systems and Signal Processing 106, 430–452. URL: https://linkinghub.elsevier.com/retrieve/pii/S0888327018300220, doi:10.1016/j.ymssp.2018.01.014.

Dickinson, M.H., Lehmann, F.O., Sane, S.P., 1999. Wing Rotation and the Aerodynamic Basis of Insect Flight. Science 284, 1954–1960. URL: http://www.sciencemag.org/cgi/doi/10.1126/science.284.5422.1954, doi:10.1126/science.284.5422.1954.

Dion, J.L., Chevallier, G., Peyret, N., 2013. Improvement of measurement techniques for damping induced by micro-sliding. Mechanical Systems and Signal Processing 34, 106–115. URL: https://linkinghub.elsevier.com/retrieve/pii/S0888327012003093, doi:10.1016/j.ymssp.2012.08.003.

Doan, L.A., Faux, D., Dupont, S., Cattan, E., Grondel, S., 2016. Modeling and simulation of the vertical take off and energy consumption of a vibrating wing nano air vehicle, in: 2016 11th France-Japan & 9th Europe-Asia Congress on Mechatronics (MECATRONICS) /17th International Conference on Research and Education in Mechatronics (REM), IEEE, Compiègne, France. pp. 123–128. URL: http://ieeexplore.ieee.org/document/7547127/, doi:10.1109/MECATRONICS.2016.7547127.

Doughty, T., Davies, P., Bajaj, A., 2002. A Comparison of Three Techniques Using Steady-state Data to Identify Nonlinear Modal Behavior of an Externally Excited Cantilever Beam. Journal of Sound and Vibration 249, 785–813. URL: http://linkinghub.elsevier.com/retrieve/pii/S0022460X01939124, doi:10.1006/jsvi.2001.3912.

Egorov, A., Kamalutdinov, A., Nuriev, A., 2018. Evaluation of aerodynamic forces acting on oscillating cantilever beams based on the study of the damped flexural vibration of aluminium test samples. Journal of Sound and Vibration 421, 334–347. URL: https://linkinghub.elsevier.com/retrieve/pii/S0022460X18300944, doi:10.1016/j.jsv.2018.02.006.

Eichler, A., Moser, J., Chaste, J., Zdrojek, M., Wilson-Rae, I., Bachtold, A., 2011. Nonlinear damping in mechanical resonators made from carbon nanotubes and graphene. Nature Nanotechnology 6, 339–342. URL: http://www.nature.com/articles/nnano.2011.71, doi:10.1038/nnano.2011.71.

Elliott, S.J., Tehrani, M.G., Langley, R.S., 2015. Nonlinear damping and quasi-linear modelling. Philosophical Transactions of the Royal Society A: Mathematical, Physical and Engineering Sciences 373, 20140402. URL: http://rsta.royalsocietypublishing.org/lookup/doi/10.1098/rsta.2014.0402, doi:10.1098/rsta.2014.0402.

Faux, D., Thomas, O., Cattan, E., Grondel, S., 2018. Two modes resonant combined motion for insect wings kinematics reproduction and lift generation. EPL 121. URL: http://stacks.iop.org/0295-5075/121/i=6/a=66001?key=crossref.24948e7f14e4c9f902a6242bd8df7398, doi:10.1209/0295-5075/121/66001.

Faux, D., Thomas, O., Grondel, S., Cattan, E., 2019. Dynamic simulation and optimization of artificial insect-sized flapping wings for a bioinspired kinematics using a two resonant vibration modes combination. Journal of Sound and Vibration URL: https://linkinghub.elsevier.com/retrieve/pii/S0022460X19304456, doi:10.1016/j.jsv.2019.114883.

Fry, S.N., Sayaman, R., Dickinson, M.H., 2003. The Aerodynamics of Free-Flight Maneuvers in Drosophila. Science 300, 495–498.

Gottlieb, O., Habib, G., 2012. Non-linear model-based estimation of quadratic and cubic damping mechanisms governing the dynamics of a chaotic spherical pendulum. Journal of Vibration and Control 18, 536–547. URL: http://journals.sagepub.com/doi/10.1177/1077546310395969, doi:10.1177/1077546310395969.

Guillot, L., Cochelin, B., Vergez, C., 2019. A Taylor series-based continuation method for solutions of dynamical systems. Nonlinear Dynamics URL: https://doi.org/10.1007/s11071-019-04989-5, doi:10.1007/s11071-019-04989-5.

Guillot, L., Lazarus, A., Thomas, O., Vergez, C., Cochelin, B., . A purely frequency based Floquet-Hill formulation for the efficient stability computation of periodic solutions of ordinary differential systems. Journal of Computational Physics In press.

Géradin, M., Rixen, D.J., 1994. Mechanical Vibrations: Theory and application to structural dynamics. Wiley.

Haddara, M., 1973. On nonlinear rolling of ships in random seas. International Shipbuilding Progress 20, 377–387. URL: http://www.medra.org/servlet/aliasResolver?alias=iospress&doi=10.3233/ISP-1973-2023001, doi:10.3233/ISP-1973-2023001.

Hao, Z., Erbil, A., Ayazi, F., 2003. An analytical model for support loss in micromachined beam resonators with in-plane flexural vibrations. Sensors and Actuators A: Physical 109, 156–164. URL: http://linkinghub.elsevier.com/retrieve/pii/S0924424703004898, doi:10.1016/j.sna.2003.09.037.

Hosaka, H., Itao, K., 1999. Theoretical and Experimental Study on Airflow Damping of Vibrating Microcantilevers. Journal of Vibration and Acoustics 121, 64. URL: http://VibrationAcoustics.asmedigitalcollection.asme.org/article.aspx?articleid=1470120, doi:10.1115/1.2893949.

Hosaka, H., Itao, K., Kuroda, S., 1995. Damping characteristics of beam-shaped micro-oscillators. Sensors and Actuators A: Physical , 87–95.

Kerschen, G., Worden, K., Vakakis, A.F., Golinval, J.C., 2006. Past, present and future of nonlinear system identification in structural dynamics. Mechanical Systems and Signal Processing 20, 505–592. URL: https://linkinghub.elsevier.com/retrieve/pii/S0888327005000828, doi:10.1016/j.ymssp.2005.04.008.

Keulegan, G.H., Carpenter, L.H., 1958. Forces on cylinders and plates in an oscillating fluid. J. RES. NATL. BUR. STAN. 60, 423–440. URL: https://nvlpubs.nist.gov/nistpubs/jres/60/jresv60n5p423_A1b.pdf, doi:10.6028/jres.060.043.

Krauss, R.W., Nayfeh, A.H., 1999. Experimental Nonlinear Identification of a Single Mode of a Transversely Excited Beam. Nonlinear Dynamics 18, 69–87.

Lacarbonara, W., Yabuno, H., 2006. Refined models of elastic beams undergoing large in-plane motions: Theory and experiment. International Journal of Solids and Structures 43, 5066–5084. URL: https://linkinghub.elsevier.com/retrieve/pii/S0020768305004877, doi:10.1016/j.ijsolstr.2005.07.018.

Lazarus, A., Thomas, O., 2010. A harmonic-based method for computing the stability of periodic solutions of dynamical systems. Comptes Rendus de l'Académie des Sciences 338, 510–517. URL: https://linkinghub.elsevier.com/retrieve/pii/S1631072110001142, doi:10.1016/j.crme.2010.07.020.

Le Rouzic, J., Delobelle, P., Vairac, P., Cretin, B., 2009. Comparison of three different scales techniques for the dynamic mechanical characterization of two polymers (PDMS and SU8). The European Physical Journal Applied Physics 48, 11201. URL: http://www.epjap.org/10.1051/epjap/2009124, doi:10.1051/epjap/2009124.

Malatkar, P., Nayfeh, A.H., 2003. A Parametric Identification Technique for Single-Degree-of-Freedom Weakly Nonlinear Systems with Cubic Nonlinearities. Modal Analysis 9, 317–336. URL: http://journals.sagepub.com/doi/10.1177/107754603030754, doi:10.1177/107754603030754.

Naeli, K., Brand, O., 2009. Dimensional considerations in achieving large quality factors for resonant silicon cantilevers in air. Journal of Applied Physics 105, 014908. URL: http://aip.scitation.org/doi/10.1063/1.3062204, doi:10.1063/1.3062204.

Nayfeh, A.H., 1985. Parametric Identification of Nonlinear Dynamic Systems. Computers & Structures 20, 487–493.

Nayfeh, A.H., Mook, D.T., 1979. Nonlinear Oscillations. Wiley and Sons.

Nouira, H., Foltête, E., Hirsinger, L., Ballandras, S., 2007. Investigation of the effects of air on the dynamic behavior of a small cantilever beam. Journal of Sound and Vibration 305, 243–260. URL: http://linkinghub.elsevier.com/retrieve/pii/S0022460X07002325, doi:10.1016/j.jsv.2007.04.013.

Pai, P.F., Nayfeh, A.H., 1990. Non-linear non-planar oscillations of a cantilever beam under lateral base excitations. International Journal of Non-Linear Mechanics 25, 455–474. URL: http://linkinghub.elsevier.com/retrieve/pii/002074629090012X, doi:10.1016/0020-7462(90)90012-X.

Pedersen, C.B., Żbikowski, R., 2006. An indicial-Polhamus aerodynamic model of insect-like flapping wings in hover, in: Liebe, R. (Ed.), Flow Phenomena in Nature: a Challenge to Engineering Design. WIT Press, Billerica, MA. volume 4 of WIT Transactions on State of the Art in Science and Engineering, pp. 606–665. URL: http://library.witpress.com/viewpaper.asp?pcode=1845640950-605-1, doi:10.2495/1-84564-095-0/6e.

Phan, C.N., Aureli, M., Porfiri, M., 2013. Finite amplitude vibrations of cantilevers of rectangular cross sections in viscous fluids. Journal of Fluids and Structures 40, 52–69. URL: https://linkinghub.elsevier.com/retrieve/pii/S0889974613000856, doi:10.1016/j.jfluidstructs.2013.03.013.

Ramananarivo, S., Godoy-Diana, R., Thiria, B., 2011. Rather than resonance, flapping wing flyers may play on aerodynamics to improve performance. Proceedings of the National Academy of Sciences 108, 5964–5969. URL: http://www.pnas.org/cgi/doi/10.1073/pnas.1017910108, doi:10.1073/pnas.1017910108.

Rhoads, J., Shaw, S.W., Turner, K.L., 2008. Nonlinear Dynamics and its Applications in Micro- and Nanoresonators. Journal of Dynamic Systems, Measurement, and Control 132, 31.

Sabater, A., Rhoads, J., 2017. Parametric system identification of resonant micro/nanosystems operating in a nonlinear response regime. Mechanical Systems and Signal Processing 84, 241–264. URL: https://linkinghub.elsevier.com/retrieve/pii/S0888327016301650, doi:10.1016/j.ymssp.2016.06.003.

Sane, S.P., Dickinson, M.H., 2001. The control of Flight Force by a Flapping Wing: Lift and drag production by a flapping wing. Journal of Experimental Biology 204, 2607–2626.

Schmid, S., Hierold, C., 2008. Damping mechanisms of single-clamped and prestressed double-clamped resonant polymer microbeams. Journal of Applied Physics 104, 093516. URL: http://aip.scitation.org/doi/10.1063/1.3008032, doi:10.

1063/1.3008032.

Crespo da Silva, M.R.M., Glynn, C.C., 1978. Nonlinear Flexural-Flexural-Torsional Dynamics of Inextensional Beams. I. Equations of Motion. Journal of Structural Mechanics 6, 437–448. URL: https://www.tandfonline.com/doi/full/10.1080/03601217808907348, doi:10.1080/03601217808907348.

Stokes, G.G., 1851. On the effect of the internal friction of fluids on the motion of pendulums. Transactions of the Cambridge Philosophical Society 9, 8–106.

Thomas, O., Sénéchal, A., Deü, J.F., 2016. Hardening/softening behavior and reduced order modeling of nonlinear vibrations of rotating cantilever beams. Nonlinear Dynamics 86, 1293–1318. URL: http://link.springer.com/10.1007/s11071-016-2965-0, doi:10.1007/s11071-016-2965-0.

Thomas, O., Touzé, C., Chaigne, A., 2003. Asymmetric non-linear forced vibrations of free-edge circular plates. Part II: experiments. Journal of Sound and Vibration 265, 1075–1101. URL: http://linkinghub.elsevier.com/retrieve/pii/S0022460X0201564X, doi:10.1016/S0022-460X(02)01564-X.

Thomas, O., Touzé, C., Luminais, E., 2007. Non-linear vibrations of free-edge thin spherical shells: Experiments on a 1:1:2 internal resonance. Nonlinear Dynamics 49, 259–284. URL: http://link.springer.com/10.1007/s11071-006-9132-y, doi:10.1007/s11071-006-9132-y.

Touzé, C., Thomas, O., Amabili, M., 2011. Transition to chaotic vibrations for harmonically forced perfect and imperfect circular plates. International Journal of Non-Linear Mechanics 46, 234–246. URL: https://linkinghub.elsevier.com/retrieve/pii/S0020746210001368, doi:10.1016/j.ijnonlinmec.2010.09.004.

Touzé, C., Thomas, O., Chaigne, A., 2004. Hardening/softening behaviour in non-linear oscillations of structural systems using non-linear normal modes. Journal of Sound and Vibration 273, 77–101. URL: https://linkinghub.elsevier.com/retrieve/pii/S0022460X03010083, doi:10.1016/j.jsv.2003.04.005.

Vakilinejad, M., Grolet, A., Thomas, O., 2020. A comparison of robustness and performance of linear and nonlinear Lanchester dampers. Nonlinear Dyn URL: http://link.springer.com/10.1007/s11071-020-05512-x, doi:10.1007/s11071-020-05512-x.

Varoto, P.S., de Oliveira, L.P.R., 2002. On the Force Drop Off Phenomenon in Shaker Testing in Experimental Modal Analysis. Shock and Vibration 9, 165–175. URL: http://www.hindawi.com/journals/sv/2002/675674/abs/, doi:10.1155/2002/675674.

Younis, M.I., 2010. MEMS linear and nonlinear statics and dynamics. volume 20 of *Microsystems*. Springer Science+Business Media, New York ; London.

Zaitsev, S., Shtempluck, O., Buks, E., Gottlieb, O., 2012. Nonlinear damping in a micromechanical oscillator. Nonlinear Dynamics 67, 859–883. URL: http://link.springer.com/10.1007/s11071-011-0031-5, doi:10.1007/s11071-011-0031-5.

Zhang, L., Hu, X., Xie, Z., 2019. Identification method and application of aerodynamic damping characteristics of super high-rise buildings under narrow-band excitation. Journal of Wind Engineering and Industrial Aerodynamics 189, 173–185. URL: https://linkinghub.elsevier.com/retrieve/pii/S0167610518311036, doi:10.1016/j.jweia.2019.03.027.

A. Aerodynamic drag force

In order to account for the action of air on the structure, a local term should be added in Eq. (15), of the form $\dot{w}|\dot{w}|$. Assuming $\dot{w}_e$ is negligible compared to $\dot{w}_r$, this term leads in Eq. (21) to an additional term of the form:

$$\sum_{i=1}^{+\infty} \dot{q}_i(\bar{t}) \int_0^1 \Phi_k(\bar{x})\Phi_i(\bar{x}) \left| \sum_{j=1}^{+\infty} \Phi_j(\bar{x})\dot{q}_j(\bar{t}) \right| \mathrm{d}x. \tag{44}$$

Using the single-mode approximation, one recovers Eq. (23). Otherwise, the drag produces a global nonlinear quadratic coupling between the modes, whose spatial dependence cannot be separated from the time dependence. In the case of base excitation, if the assumption $\dot{w}_e \ll \dot{w}_r$ is not verified, then the excitation motion cannot be pulled out of the absolute value and the term of Eq. (44) is even more complex.

B. Method of multiple scales

In this section, the oscillator equation is the following:

$$\ddot{q} + 2\xi\omega_0\dot{q} + \omega_0^2 q + \nu_1\dot{q}|\dot{q}| + \nu_2\dot{q}^3 + \nu_3 q^2\dot{q} + \Gamma q^3 + \Pi(\ddot{q}q^2 + \dot{q}^2 q) = F\cos(\Omega\bar{t}). \tag{45}$$

In order to use the method of multiple scales [Nayfeh and Mook [1979]], the terms in Eq. (45) are adjusted in powers of ϵ, a book-keeping parameter, to have a valid analytical solution:

$$\ddot{q} + \omega_0^2 q = -\epsilon 2\xi\omega_0\dot{q} - \epsilon\nu_1\dot{q}|\dot{q}| - \epsilon\nu_2\dot{q}^3 - \epsilon\nu_3 q^2\dot{q} - \epsilon\Gamma q^3 - \epsilon\Pi(\ddot{q}q^2 + \dot{q}^2 q) + \epsilon F\cos(\Omega\bar{t}), \tag{46}$$

First, new time variables are introduced:

$$T_n = \epsilon^n \bar{t}, \forall n \in \mathbb{N}, \tag{47}$$

which leads to the following expressions of the partial derivatives with respect to the T_n:

$$\frac{\mathrm{d}}{\mathrm{d}\bar{t}} = D_0 + \epsilon D_1 + \epsilon^2 D_2 + ..., \tag{48}$$

$$\frac{\mathrm{d}^2}{\mathrm{d}\bar{t}^2} = D_0^2 + 2\epsilon D_0 D_1 + \epsilon^2 (D_1^2 + 2D_0 D_2) + ... \tag{49}$$

where $D_n = \frac{\partial}{\partial T_n}$. Then, q is developed in powers of ϵ:

$$q(\bar{t}) = q_0(T_0, T_1, T_2, ...) + \epsilon q_1(T_0, T_1, T_2, ...) + \epsilon^2 q_2(T_0, T_1, T_2, ...)... \tag{50}$$

Substituting Eq. (50) into Eq. (46) and equating the coefficients of ϵ to zero, we obtain:

$$D_0^2 q_0 + \omega_0^2 q_0 = 0, \tag{51}$$

$$\begin{aligned} D_0^2 q_1 + \omega_0^2 q_1 = & - 2D_0 D_1 q_0 - 2\xi\omega_0 D_0 q_0 \\ & - \nu_1 D_0 q_0 |D_0 q_0| - \nu_2 (D_0 q_0)^3 - \nu_3 q_0^2 (D_0 q_0) \\ & - \Gamma q_0^3 - \Pi((D_0 q_0)^2 q_0 + D_0^2 q_0 q_0^2) + F\cos(\Omega T_0). \end{aligned} \tag{52}$$

Equation (51) leads to a solution q_0 of the form:

$$q_0 = A(T_1)e^{j\omega_0 T_0} + cc, \tag{53}$$

with cc referring to the complex conjugate of what precedes in the right-hand side of the equation. Focusing on the primary resonance of the system, we set the detuning parameter such that $\Omega = \omega_0 + \epsilon\sigma$. Substituting Eq. (53) into Eq. (52) gives:

$$\begin{aligned} D_0^2 q_1 + \omega_0^2 q_1 = & - A^2 \bar{A}(3\Gamma - 2\omega_0^2 \Pi)e^{j\omega_0 T_0} - 2j\omega_0(D_1 A + A\xi\omega_0 + (\frac{3}{2}\nu_2 \omega_0^2 + \frac{1}{2}\nu_3)A^2\bar{A})e^{j\omega_0 T_0} \\ & - (\Gamma - 2\omega_0^2 \Pi)A^3 e^{3j\omega_0 T_0} + j(\nu_2 \omega_0^3 - \nu_3 \omega_0)A^3 e^{3j\omega_0 T_0} + \frac{F}{2}e^{j(\omega_0 T_0 + \sigma T_1)} + cc \\ & - \omega_0^2 \nu_1 j(Ae^{j\omega_0 T_0} - \bar{A}e^{-j\omega_0 T_0})|j(Ae^{j\omega_0 T_0} - \bar{A}e^{-j\omega_0 T_0})|. \end{aligned} \tag{54}$$

Eliminating the secular terms from Eq. (54) requires all terms in the right-hand side of the equation proportional to $e^{j\omega_0 T_0}$ to be zero. For the last term of Eq. (54), we develop it into Fourier series and calculate the first harmonic's amplitude to set it to zero (we note $\tau = \omega_0 T_0$):

$$\begin{aligned} 0 = & - 2j\omega_0(D_1 A + A\xi\omega_0 + (\frac{3}{2}\nu_2 \omega_0^2 + \frac{1}{2}\nu_3)A^2\bar{A}) - A^2\bar{A}(3\Gamma - 2\omega_0^2 \Pi) + \frac{F}{2}e^{j(\sigma T_1)} \\ & - \frac{j\omega_0^2 \nu_1}{2\pi} \int_0^{2\pi} (Ae^{j\tau} - \bar{A}e^{-j\tau})|j(Ae^{j\tau} - \bar{A}e^{-j\tau})|e^{-j\tau}\mathrm{d}\tau. \end{aligned} \tag{55}$$

Now, expressing A in the polar form $(A(T_1) = \frac{1}{2}ae^{j\beta(T_1)})$ and switching variable $\phi = \tau + \beta$ [Anderson et al. [1996]], yields:

$$\begin{aligned} 0 = & \left(2\omega_0 a \frac{\partial\beta}{\partial T_1} - 2\omega_0 j(\frac{\partial a}{\partial T_1} + a\xi\omega_0 + \frac{a^3}{16}(3\nu_2 \omega_0^2 + \nu_3)) - \frac{3\Gamma - 2\Pi\omega_0^2}{8}a^3 \right) e^{j\beta} \\ & + \frac{F}{2}e^{\sigma T_1} + \frac{\omega_0^2 \nu_1}{2\pi}a^2 \int_\beta^{2\pi+\beta} \underbrace{\sin\phi|\sin\phi|e^{-j\phi}}_{f(\phi)}\mathrm{d}\phi \, e^{j\beta}. \end{aligned}$$

As $f(\phi)$ is 2π-periodic, we have $\int_0^t f(\phi)\mathrm{d}\phi = \int_{2\pi}^{2\pi+t} f(\phi)\mathrm{d}\phi$ and one can calculate $\int_0^{2\pi} f(\phi)\mathrm{d}\phi = -\frac{8j}{3}$. Multiplying by $e^{-j\beta}$, and separating real and imaginary parts in the previous equation leads to:

$$
\begin{cases}
a\frac{\partial\beta}{\partial T_1} = \frac{3\Gamma-2\Pi\omega_0^2}{8\omega_0}a^3 - \frac{F}{2\omega_0}\cos(\sigma T_1 - \beta) & = 0 \\
\frac{\partial a}{\partial T_1} = -a(\xi\omega_0 + \frac{4}{3\pi}\omega_0\nu_1 a + (\frac{3}{8}\omega_0^2\nu_2 + \frac{1}{8}\nu_3)a^2) + \frac{F}{2\omega_0}\sin(\sigma T_1 - \beta) & = 0
\end{cases}
\tag{56}
$$

Let $\gamma = \sigma T_1 - \beta$. Furthermore, being in steady-state regime comes down to $\frac{\partial a}{\partial T_1} = \frac{\partial \gamma}{\partial T_1} = 0$. Eq. (56) is now:

$$
\begin{cases}
a\sigma - \frac{(3\Gamma - 2\omega_0^2\Pi)}{8\omega_0}a^3 & = -\frac{F}{2\omega_0}\cos\gamma, \\
\xi\omega_0 a + \frac{4}{3\pi}\nu_1\omega_0 a^2 + (\frac{3}{8}\omega_0^2\nu_2 + \frac{1}{8}\nu_3)a^3 & = \frac{F}{2\omega_0}\sin\gamma
\end{cases}
$$

The forced response of the system in steady-state can be obtained from:

$$
\Omega - \omega_0 = \frac{(3\Gamma - 2\omega_0^2\Pi)}{8\omega_0}a^2 \pm \sqrt{\frac{F^2}{4\omega_0^2 a^2} - \omega_0^2\left(\xi + \frac{4\nu_1}{3\pi}a + (\frac{3\omega_0\nu_2}{8} + \frac{\nu_3}{8\omega_0})a^2\right)^2}.
\tag{57}
$$

Note: Given the fact that the nonlinear function related to the aerodynamic damping in the oscillator equation (Eq. (45)) presents a central symmetry, the constant value and the even harmonics of the solution are zero (see the appendix of [Vakilinejad et al. [2020]]), although this term presents a quadratic nonlinearity. Surely, in Eq. (54), there are no constant value or harmonic of order 2. Indeed, one can verify that the constant value and the Fourier series coefficient of the second harmonic of the term $-j\omega_0^2\nu_1(Ae^{j\tau} - \bar{A}e^{-j\tau})|(Ae^{j\tau} - \bar{A}e^{-j\tau})|$ are zero.

C. Manlab implementation of the nonlinear equations

In the framework of MANlab, the problem to solve must be written under the form of a first-order dynamical system with quadratic nonlinearities only [Guillot et al.]. As Eq. (39) is a simplified version of Eq. (40), the latter only is detailed here. We introduce $r = \dot{q}$ to transform Eq. (40) into the first order dynamical system:

$$
\dot{q} = r
\tag{58}
$$
$$
\dot{r} = F\cos(\Omega t) - (2\xi r + q + \nu r|r| + \Gamma q^3).
$$

We introduce two more variables $s = q^2$ and $u = |\dot{q}| = |r|$. This last equation is non-smooth so we replace it by a regularised version $\delta = r^2 - u^2$, with δ the regularisation parameter chosen as small as possible. In practice, convergence tests demonstrated that $\delta = 0.001$ was low enough. The problem can now be expressed as the following first-order dynamical system with quadratic nonlinearities only:

$$
\dot{q} = r,
\tag{59}
$$
$$
\dot{r} = F\cos(\Omega t) - 2\xi r - q - \nu r u - \Gamma q s,
$$
$$
0 = s - q^2,
$$
$$
0 = \delta - r^2 + u^2.
$$

It is necessary to initialise MANlab with a starting point: we choose the linear solution $q_l = F/(1 - \Omega^2 + 2i\xi\Omega)$. We set a starting frequency at $\Omega = 0.01$. The starting point is described with the Fourier coefficients of q, r, s and u: $q_{\cos} = \mathrm{Re}(q_l)$, $q_{\sin} = -\mathrm{Im}(q_l)$, $r_{\cos} = \Omega q_{\sin}$, $r_{\sin} = -\Omega q_{\cos}$, $s_0 = q_{\cos}^2/2 + q_{\sin}^2/2$, $s_{2\cos} = q_{\cos}^2/2 - q_{\sin}^2/2$, $s_{2\sin} = q_{\cos}q_{\sin}$, $u_0 = 2\Omega|q_{\cos}|/\pi$, and $u_{2\cos} = -\Omega|q_{\cos}|4/(3\pi)$. The other parameters values are $\xi = 0.001$, $\nu = 0.03\pi/4$, and F varies between 0.0005 and 0.005.

D. Phase of the simulated frequency responses with MANlab

In Fig. 12, the phase variation at the vicinity of the resonance is reduced – it becomes more and more "flat" – as the forcing increases.
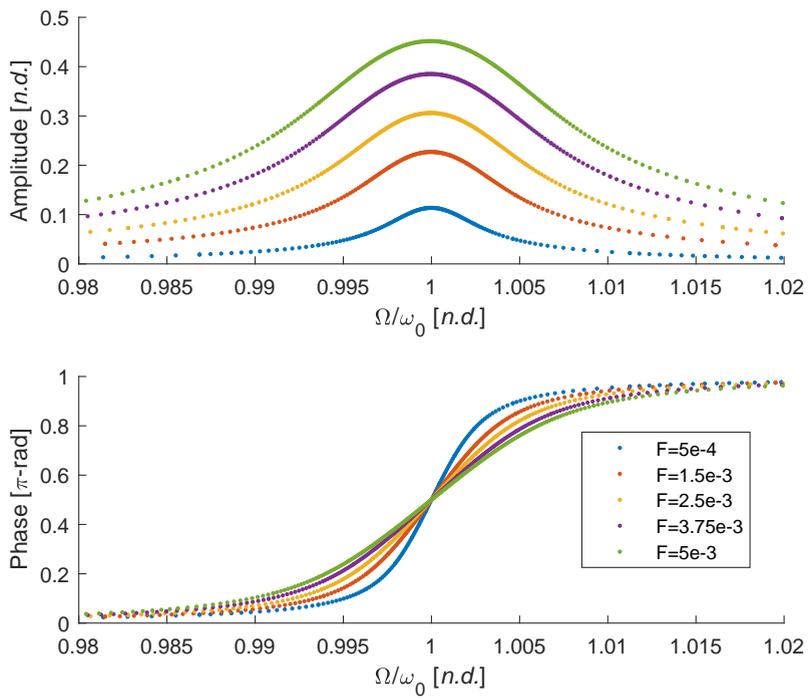
Figure 12: Simulated frequency responses with MANlab